Modelling argon dynamics in first-year sea ice

Sébastien Moreau[1*], Martin Vancoppenolle[2,1], Jiayun Zhou[3], Jean-Louis Tison[3], Bruno Delille[4], Hugues Goosse[1]

[1] Georges Lemaître Centre for Earth and Climate Research, Earth and Life Institute, Université catholique de Louvain, Louvain-La-Neuve, Belgium.

[2] Laboratoire d'Océanographie et du Climat, CNRS, Paris, France.

[3] Laboratoire de Glaciologie, Faculté des Sciences, Université Libre de Bruxelles, 50 Avenue F.D. Roosevelt, 1050 Bruxelles, Belgium.

[4] Unité d'océanographie chimique, MARE, Université de Liège, Belgium.

* Corresponding author email:s.moreau@uclouvain.be

Abstract

Focusing on physical processes, we aim at constraining the dynamics of argon (Ar), a biogeochemically inert gas, within first year sea ice, using observation data and a one-dimensional halo-thermodynamic sea ice model, including parameterization of gas physics. The incorporation and transport of dissolved Ar within sea ice and its rejection via gas-enriched brine drainage to the ocean, are modeled following fluid transport equations through sea ice. Gas bubbles nucleate within sea ice when Ar is above saturation and when the total partial pressure of all three major atmospheric gases (N_2, O_2 and Ar) is above the brine hydrostatic pressure. The uplift of gas bubbles due to buoyancy is allowed when the brine network is connected with a brine volume above a given threshold. Ice-atmosphere Ar fluxes are formulated as a diffusive process proportional to the differential partial pressure of Ar between brine inclusions and the atmosphere. Two simulations corresponding to two case studies that took place at Point Barrow (Alaska, 2009) and during an ice-tank experiment (INTERICE IV, Hamburg, Germany, 2009) are presented. Basal entrapment and vertical transport due to brine motion enable a qualitatively sound representation of the vertical profile of the total Ar (i.e. the Ar dissolved in brine inclusions and contained in gas bubbles; *TAr*). Sensitivity analyses suggest that gas bubble nucleation and rise are of most importance to describe gas dynamics within sea ice. Ice-atmosphere Ar fluxes and the associated parameters do not drastically change the simulated *TAr*. Ar dynamics are dominated by uptake, transport by brine dynamics and bubble nucleation in winter and early spring; and by an intense and rapid release of gas bubbles to the atmosphere in spring. Important physical processes driving gas dynamics in sea ice are identified, pointing to the need for further field and experimental studies.

Keywords: Argon, Sea ice, Modelling, Gas bubbles, Gas exchange

1. Introduction

Sea ice is an important component of the Earth System. First, sea ice is a sensitive indicator of climate change, as witnessed by its rapid retreat in the Arctic (Comiso and Nishio, 2008; Lindsay and Zhang, 2005; Serreze et al., 2007) and from the waters west of the Antarctic Peninsula (Stammerjohn et al., 2008). Sea ice also influences climate due to its high albedo, its insulating effect that reduces the underlying water heat loss in winter and its influence on the water column stratification in Polar Regions, driving the global thermohaline circulation (Goosse and Fichefet, 1999; Randall et al., 2007). Sea ice may also play an important, but still mainly unresolved, role in the sequestration of greenhouse gases by the ocean. Rysgaard et al. (2011) estimated that the seasonal CO_2 uptake in the sea ice zone may equal half of the annual CO_2 uptake of ice-free polar seas. The role of sea ice on CO_2 dynamics in the Polar Oceans has so far not been properly represented in global Earth System models, because in those models sea ice is considered as an impervious shield preventing ocean-atmosphere gas exchanges (Yager et al., 1995). Recently, however, active gas sources and sinks in sea ice, as well as dynamic gas transport through the sea ice brine network have been evidenced (e.g. Delille et al., 2007; Geilfus et al., 2012; Mock et al., 2002; Papadimitriou et al., 2003; Semiletov et al., 2004; Tison et al., 2010). Biogeochemical processes, including the photosynthesis and respiration of microbial assemblages thriving in sea ice actively contribute to gas dynamics (Arrigo et al., 2010; Deming, 2010; Gleitz et al., 1995), but their proper quantification has still to come.

As the observation of gas exchanges through sea ice is a real challenge, modelling can help to provide theoretical constraints on the syngenetic, epigenetic and exogenetic processes that govern gas dynamics within sea ice (Tsurikov, 1979). The processes associated with ice formation, whatever the mode of formation (wind and wave turbulence frazil ice, congelation

growth of columnar ice, snow ice, superimposed ice) are referred to as *syngenetic* (Matsuo and Miyake, 1966). *Epigenetic* processes encompass all the phenomena that affect gas content and composition from within the sea ice. This includes the nucleation and dissolution of gas bubbles within sea ice associated with temperature changes (Tison et al., 2002); the vertical redistribution of dissolved gas associated with brine dynamics (Loose et al., 2011a; Tison et al., 2010) and the vertical uplift of buoyant gas bubbles (Zhou et al., submitted); the formation of gaseous inclusions due to biogeochemical sources and sinks, such as photosynthesis (Delille et al., 2007; Mock et al., 2002). The *exogenetic* processes refer to the exchanges of gas between sea ice, the atmosphere and the ocean (Nomura et al., 2010a; Papakyriakou and Miller, 2011). For the present study, we only consider the following processes: gas entrapment and gas release from solution during freezing (syngenetic), gas bubble nucleation and rise (epigenetic), and gas exchanges between sea ice, the atmosphere and the ocean (exogenetic).

Argon (Ar) is a noble gas unaffected by biological activities such as primary production, remineralization or grazing that take place within sea ice. Hence, it is often used to understand oceanic physical processes such as deep water formation (Hamme and Severinghaus, 2007), air-sea gas exchanges (Stanley et al., 2006) or processes controlling oceanic gas saturation states (Ito et al., 2011). Ar may also be used, along with oxygen which has a similar solubility (Broecker and Peng, 1974), as a potential indicator of the net community production within environments such as seawater (Nemcek et al., 2008) and sea ice (Zhou et al., in preparation). Using the O_2/Ar ratio to estimate the net community production is an advantageous non-invasive technique compared to other methods (Arrigo et al., 2010). Hence, modelling Ar is a first step towards a better understanding of the physical controls on gas dynamics within sea ice, an estimation of primary production in sea ice, and a better understanding of gas exchanges (e.g., CO_2) in ice-covered oceans.

In the present study, we attempt to identify the importance of the physical processes potentially driving gas dynamics within sea ice: gas entrapment, gas release from solution during freezing, gas bubble nucleation and rise, and gas exchanges between sea ice, the atmosphere and the ocean. To do so, a representation of the impact of those processes on Ar concentrations within first-year sea ice is implemented in a one-dimensional halo-thermodynamic sea ice model. Our analyses are based on two model simulations, run to mimic the conditions from two observation sites: Point Barrow (natural sea ice, Alaska) and INTERICE (artificial ice grown in an ice tank, HSVA, Hamburg, Germany).

2. The model

2.1. Model physics

The model presented is one-dimensional and only vertical processes are considered. We consider a horizontally uniform sea ice layer of thickness h_i and covered by a uniform layer of snow of depth h_s. The model consists of 4 components: ice halo-thermodynamics, radiative transfer, brine transport and abiotic gas dynamics. At each depth z within the ice, the brine salinity $\sigma(z)$ and brine volume fraction $e(z)$ (or brine volume) are determined from the bulk ice temperature $T(z)$ and salinity $S(z)$ (Schwerdtfeger, 1963).

In the model, sea ice forms at the ice base by congelation and melts at the surface and base of sea ice depending on interfacial heat budgets, involving atmospheric, oceanic and inner ice conductive heat fluxes (Vancoppenolle et al., 2007; 2010). Salinity and temperature control the thermal properties of sea ice (thermal conductivity, specific heat and energy of melting; see Bitz and Lipscomb, 1999). In the model, ice may also form as snow ice when snow is deep

enough to depress the ice surface below sea level. Seawater infiltrates between sea ice and the snow cover and instantaneously freezes in the snow, forming snow ice (Vancoppenolle et al., 2009). As in Vancoppenolle et al (2010), the model halodynamics are based on advection-diffusion equations. Gravity drainage is represented using a mixing term and an effective diffusivity that involves the brine volume fraction $e(z)$ and a porous-medium Rayleigh number, *Ra*, (Notz and Worster, 2008). When ice melts, fresh water percolates through the brine network (i.e. flushing) given that $e \geq 5\%$ within the entire ice column. This process is represented as an advective flow.

2.2. Gas concentrations and dynamics

Most of the syngenetic, epigenetic and exogenetic processes that we believed to be important were introduced in the model. Considering that Ar may either be dissolved in brine inclusions or present in gas bubbles, the total concentration of Ar within each control volume of sea ice, C^{TAr}, is formulated as the sum of dissolved gas and gas bubbles:

$$C^{TAr} = C^{dAr} + C^{bAr} = e\,\zeta^{dAr} + C^{bAr} \qquad \text{eq.1}$$

where C^{dAr} is the bulk dissolved fraction of Ar, e is the brine volume fraction, ζ^{dAr} is the concentration of dissolved Ar in brine (with $e * \zeta^{dAr}$ in mmol m^{-3} of ice), and C^{bAr} is the contribution of gas bubbles to bulk concentration (in mmol m^{-3} of ice).

The total gas concentration in sea ice is in general controlled by physical and biogeochemical sources and sinks. For Ar, biological sources are nil, and therefore, we assume that the brine and bubble concentrations evolve in the following way:

$$\frac{\partial(e\zeta^{dAr})}{\partial t} = \frac{\partial}{\partial z}\left(eD\frac{\partial \zeta^{dAr}}{\partial z}\right) - Q\frac{\partial \zeta^{dAr}}{\partial z} - eS^{bub} \quad \text{eq.2}$$

$$\frac{\partial C^{bAr}}{\partial t} = eS^{bub} + T^{bub} \quad \text{eq.3}$$

142

143 The first two terms on the right-hand side of eq. 2 express that the Ar dissolved in brine
144 inclusions is transported similarly to salt. The first of these two terms represents the mixing of
145 Ar by molecular diffusion and convection, while the second of these two terms represents the
146 effect of flushing as in Vancoppenolle et al. (2010). *D* is an effective diffusivity, equal to the
147 molecular (turbulent) diffusivity if *Ra* is sub (super-) critical. *Q* is the Darcy velocity associated
148 with brine flushing (Vancoppenolle et al., 2010). More precisely, we consider a flux of melt
149 water *Q* (of salinity 0) which enters the brine network through the uppermost layer of sea ice.
150 With this formulation, depending on the direction of the sea ice-ocean Ar concentration
151 gradient, Ar is either incorporated into or released from sea ice due to gravity drainage and
152 expelled from sea ice due to percolation.

153

154 The third term on the right-hand side of eq.2, S^{bub}, specifies how bubble nucleation/dissolution
155 extracts/releases *dAr* from/to the liquid phase. Brine volume fraction is present to ensure
156 conservation of total Ar concentration. Gas bubbles are assumed not to follow brine dynamics;
157 hence there are no brine transport terms in eq. 3. The same S^{bub} term releases/extracts Ar
158 into/from bubbles. A specific transport term T^{bub} accounts for buoyant gas bubble rise (see 2.4).

159

160 Finally, Ar is incorporated within sea ice through basal congelation. As in Vancoppenolle et al
161 (2010), the concentration of Ar in newly formed basal ice is assumed to be equal to the Ar
162 concentration in seawater, C_w^{Ar} (see section 2.5.1 for a description of C_w^{Ar}).

2.3. Gas bubble nucleation and dissolution

As recent observations suggest that brine concentrations of Ar are much larger than saturation (Zhou et al., submitted), we argue that the major sources and sinks of gaseous Ar in sea ice must be associated with the nucleation and dissolution of gas bubbles due to super- and under-saturation of dissolved Ar in brine inclusions.

Within the ocean, gas bubble nucleation is mainly generated by the action of breaking waves (Keeling, 1993). This process has been the focus of intensive research, modelling in particular, over the last decades. Bubble mediated gas exchanges between the ocean and the atmosphere are represented by separating two end-members: small bubbles that completely dissolve within the ocean and large bubbles that will rise back to the ocean surface, exchanging gas with the ocean during their ascent, as a function of the gas solubility and molecular diffusivity (Hamme and Emerson, 2002, 2006; Liang et al., 2011). However, the physical conditions that trigger the nucleation of gas bubbles within sea ice are not related to the action of breaking waves and another modelling approach is needed.

Very little is known about the nucleation of gas bubbles within sea ice, although their existence within sea ice has been reported (e.g. Light et al., 2003). Previous studies of gas contents within sea ice suggested that gases are found above their solubility value within sea ice (Killawee et al., 1998; Thomas et al., 2010; Tison et al., 2002). In addition, Carte (1961) and Lubetkin (2003) suggested that gas bubbles form when gas content within sea ice is above saturation. However, this process has not been represented in sea ice models so far. A recent study of sea ice microstructure performed under high resolution imagery showed that gas bubbles were only

present in the vicinity of brine inclusions (Light et al., 2003). Therefore, we only consider gas bubbles to nucleate within brine inclusions. In addition, to explicitly represent to gas bubbles would imply to model other gases present in sea ice (e.g. N_2, CO_2, CH_4 and DMS) which was not the goal of the present study. Therefore, since a realistic formulation of bubble nucleation within brine inclusions seems out of reach given the number of poorly understood processes – for instance the size distribution of gas inclusions, as well as the dependence of the Ar solubility on pressure and temperature in the brine inclusions – we designed the simplest parameterization of the nucleation/dissolution of Ar-rich gas bubbles, using a linear dependence on the level of super-/under-saturation.

The model parameterization of gas bubble nucleation and dissolution used here is the following. During ice growth, brine inclusions contract due to decreasing temperatures, and the brine concentration of gases initially dissolved in seawater increases. For some gases, including Ar, the brine concentration in dissolved gas reaches saturation and promotes the nucleation of bubbles (Killawee et al., 1998; Light et al., 2003; Tison et al., 2002) given that the total partial pressure of all three major atmospheric gases (N_2, O_2 and Ar) is above the brine hydrostatic pressure calculated as in Eide and Martin (1975). Conversely, if dissolved Ar concentration within brine inclusions becomes undersaturated, gaseous Ar from the bubbles dissolves back to the brine inclusions. Hence, the source term for bubble nucleation/dissolution reads:

$$S^{bub} = R^{bub}\left(\zeta^{dAr} - \alpha_{sat}\zeta_{sat}^{dAr}\right) \qquad \text{eq.4}$$

where R^{bub} is a prescribed rate of bubble nucleation/dissolution, given as a percentage of the supersaturation that will be converted to the gas phase each hour; and $\alpha_{sat} \geq 1$ is the ratio of supersaturation that is tolerated in brines. Those two parameters are used to control the bubble

Ar concentration, as instantaneous transfer of all supersaturation leads to rapid accumulation of Ar in gas bubbles (see Results and Discussion for details).

The concentration of Ar at saturation is calculated from the equations of Hamme and Emerson (2004) for Ar:

$$\ln\left(\zeta_{sat}^{dAr}\right) = a_0 + a_1 * T_s + a_2 * T_s^2 + a_3 * T_s^3 + \sigma * (b_0 + b_1 * T_s^2 + b_2 * T_s^3) \qquad \text{eq.5}$$

where T_s = ln[(298.15-T)/(273.15+T)] and T is the brine inclusions temperature (°C), σ is the sea ice brines salinity and with a_0 = 2.79150, a_1 = 3.17609, a_2 = 4.13116, a_3 = 4.90379, b_0 = -0.00696233, b_1 = -0.00766670 and b_2 = -0.0116888. While this fit has been developed for temperatures higher than 0 °C, we use it below this threshold, which is an approximation. In practise, as we assume thermal equilibrium in brine inclusions, brine salinity depends on temperature, and hence the solubility of Ar is only a function of temperature within sea ice.

2.4. Gas bubble rising velocity

Because of their buoyancy, gas bubbles are expected to rise within the brine network, once the latter is connected (Eide and Martin, 1975), which occurs above a certain brine volume fraction threshold. Observations suggest that gas bubble size ranges from 0.004 to 0.07 mm in radius at – 15 °C and that most bubbles are smaller than 0.2 mm during the whole sea ice season (i.e. with brine inclusions temperatures ranging from -30 to -2 °C; Gavrilo and Gaitskhoki, 1970; Grenfell, 1983; Light et al., 2003). For simplification, we only consider gas bubbles with a radius of 0.1 mm to be present within sea ice brines (Light et al., 2003). Assuming a constant bubble size and no impact of sea ice microstructure (i.e. tortuosity), it is possible to constrain the maximum gas bubble rising velocity (w) from Woolf and Thorpe (1991) as a function of their own buoyant rise speed:

$$w = \left(\frac{2\,r^2\,g}{9 * \nu}\right) * [(y^2 + 2y)^{0.5} - y] \quad \text{eq.6}$$

With $y = 10.82/\chi$, $\chi = g\,r^3 / \upsilon^2$, g the gravity (m s^{-2}), r the bubble radius (m) and ν the kinematic viscosity of brines (m^2 s^{-1}). Because "dirty" gas bubbles rise slower in the water column than "clean bubbles" (Woolf and Thorpe, 1991), the formula for "dirty" gas bubbles is used here to calculate the minimum rising velocity of gas bubbles within sea ice brines. For a bubble of radius 0.1 mm and a kinematic viscosity (ν) of 2.7 10^{-6} m^2 s^{-1} for seawater at -10 °C and a salinity of 70 g kg^{-1} and calculated from sea ice brine density (ρ) and brine dynamic viscosity (μ) as $\nu = \mu / \rho$, the rising velocity of a gas bubble within sea ice would be: 0.008 m s^{-1} or 27.9 m h^{-1}. As a comparison, within the ocean, Blanchard and Woodcock (1957) and Woolf and Thorpe (1991) reported bubble rising velocities of 0.015 m s^{-1} for bubbles with a radius of 0.1 mm. The upward bubble velocity calculated here for sea ice brines, with the formulation of Woolf and Thorpe (1991) designed for open water, is, therefore, slightly lower and seems to be a reasonable assumption. In addition, we studied the potential effect of gas-liquid drag on gas bubbles dynamics and particularly for small bubbles with low buoyancy and found that the minimum speed required for brine drainage to cancel gas bubbles buoyancy was smaller than salt, and hence brine, fluxes measured at the ice/water interface by Wakatsuchi (1983).

The formulation of Woolf and Thorpe (1991) used here is developed to describe bubble rise in open water and has been given here as a zero order approximation since no formulation is available yet for bubble rise in sea ice brines. Consequently, we do not consider here the possible interaction between gas bubbles and brine pockets sidewalls, i.e. viscous drag. In addition, we also neglect the effect of sea ice tortuosity on gas bubble rise. Because of sea ice tortuosity, some gas bubbles could be stored within an interconnected brine network and anfractuosities; which would somewhat slow down gas bubbles on their way to the atmosphere.

The values given by the formulation of Woolf and Thorpe (1991) are thus likely higher than the ones experienced by bubbles in sea ice. Observations by Zhou et al. (submitted) suggest that ice is permeable to gas release near a 10% brine volume fraction threshold. This observation probably reflects the impact of sea ice tortuosity and/or viscous drag on gas bubble rise. Therefore, for simplicity, and in the absence of a complete understanding in the literature of the interactions between different bubbles or with brine pockets sidewalls, gas bubble rise only depends on brine volume here.

Considering the time step of the model (i.e. 3600 s, see below), the potential gas bubble rise speed calculated previously and the fact that we study landfast first year sea ice with a maximum depth < 2 m, it is appropriate to think that gas bubble would readily escape sea ice when brine inclusions are connected with a brine volume above a given threshold. In practice, T^{bub} – representing the impact of gas bubble rise on gaseous Ar – is computed in the following way. When the brine volume fraction is above a prescribed threshold (e.g. e_T^{gas} = 10%), all gas bubbles are assumed to instantaneously rise up to the atmosphere, or stop on the way when they encounter a layer with e < e_T^{gas}. Therefore, gas bubbles can be stored within the ice until they have a direct connection with the atmosphere.

2.5. Gas exchange between sea ice, the ocean and the atmosphere

2.5.1. Gas exchange between sea ice and the ocean

At the base of sea ice, we assume the continuity of dissolved gas concentration between seawater and brine and impose a Dirichlet condition: $\zeta^{dAr} = C_w^{Ar}$, where C_w^{Ar} is the concentration of Ar in seawater. As Hamme and Emerson (2002) state that Ar concentrations

within the ocean are found to be close to saturation (± 2%) , we consider surface water Ar concentrations to be constant. The concentration of Ar in surface water is taken as:

$$C_w^{Ar} = f_{air}^{Ar} \Sigma^{Ar} \quad \text{eq.7}$$

where Σ^{Ar} is the solubility of Ar (mol Pa^{-1} m^{-3}) and is a function of temperature and salinity and f_{air}^{Ar} is the fugacity of Ar in the atmosphere. We assume that Ar is an ideal gas, with low molecular weight; hence, fugacity reduces to pressure. Ar contribution to atmospheric composition is 0.934% expressed as the ratio of moles of Ar to the total number of moles of gas in dry air (see Sarmiento and Gruber, 2006, Table 3.1.1 p. 74). Hence, as partial pressures and molar concentrations are proportional: $f_{air}^{Ar} = p_{atm} * 0.00934$, with p_{atm} the atmospheric pressure. Because, the concentration of Ar in surface water is close to equilibrium with the atmosphere, at a pressure of 1 atmosphere, there is 0.018 mol m^{-3} of Ar dissolved in surface sea waters which seems a reasonable assumption compared to Kakayama et al. (2002) who observed Ar concentration between 0.017 and 0.018 mol m^{-3} in the north Pacific with water temperatures ranging from -1 to 1 ºC.

2.5.2. **Gas exchange between sea ice and the atmosphere**

At the surface of sea ice, we impose a flux boundary condition where:

$$F^{Ar} = k^{Ar} * a_{eff} * (\Sigma^{Ar} f_{air}^{Ar} - \zeta^{dAr}) \quad \text{eq.8}$$

This equation expresses that the brine concentration of dissolved Ar will tend to reach equilibrium with the atmosphere at a rate which depend on k^{Ar}, the piston velocity (m s^{-1}). expresses the fraction of the sea ice surface occupied by brines. By default, $a_{eff} = R_b\, e$, where R_b is the brine aspect ratio. R_b is equal to 1 for isotropic brines and < 1 if brines are vertical ellipsoids. Here, we will assume isotropic brine inclusions near the ice surface and assume a_{eff}

299 = e,. Equation 8 describes the flux of dissolved Ar between sea ice brines and the atmosphere
300 and does not include gas bubble flux (as described in section 2.4).

301

302 We consider a "stagnant film" molecular diffusion of Ar between the brine openings on the top
303 layer of sea-ice and the atmosphere as in Gat and Shatkay (1991). The piston velocity is
304 directly proportional to D, the molecular diffusion coefficient of gas in the liquid phase and z_{BL},
305 the thickness of the diffusive boundary layer:

$$k^{Ar} = D \,/\, z_{BL} \qquad \text{eq.9}$$

306 Zemmelink et al. (2008; 2006) noticed gradients in CO_2 and dimethylsulfide (DMS) in the
307 snow cover above sea ice in the Weddell Sea, arguing for the role of the snow cover in gas
308 exchanges between sea ice and the atmosphere. However, for simplification, this present
309 parameterization assumes that snow has no impact on gas exchanges between sea-ice and the
310 atmosphere.

311

312 **2.6. Numerics**

313 The salt and gas transport equations are solved within the framework of a 10 layer
314 thermodynamic sea ice model (see Figure 1 of Vancoppenolle et al., 2010 for a sketch of the
315 model grid) and using a finite difference, implicit numerical scheme to ensure salt and gas mass
316 conservation to computer precision. The thickness of sea ice layers changes in time with ice
317 growth and melt. At each time step, the changes in ice temperature, salinity and thickness are
318 computed, giving S^{n+1} and T^{n+1}; followed by the computation of the Argon concentration
319 change. The time stepping of this procedure is the following. New brine volume e^{n+1} for each
320 layer is diagnosed from S^{n+1} and T^{n+1}. The role of changing brine volume on Ar concentrations
321 is accounted for by initializing ζ_*^{dAr} as:

$$\zeta_*^{dAr} = C_n^{dAr} / e_{n+1} \quad \text{eq.10}$$

322 Then, Argon transport (eq. 2) is solved for ζ, giving ζ_*, keeping e fixed, and the bulk
323 dissolved concentration of Argon is recomputed using:

$$C_{n+1}^{dAr} = \zeta_*^{dAr} * e_{n+1} \quad \text{eq.11}$$

324 Sources of new ice argon are then computed. This method ensures the conservation of
325 tracer contents summed over the sea ice-snow column within computer precision. The total
326 argon content is given in kg m^{-2} by:

$$M^c = \sum_{k=1}^{n} C_k \Delta z_k \quad \text{eq.12}$$

327 The computation of T_k, S_k and C_k for all layers k ($k = 1, \ldots, N$) within the computer code
328 follows the under mentioned procedure: (1) radiative transfer; (2) diffusion of heat; (3) salt
329 transport; (4) gas transport; (5) gas sources and sinks; (6) ice growth and melt; (7) vertical
330 remapping for salt, enthalpy and gas concentration.

331

332 ## 3. Experimental Setup

333 ### 3.1. Observations used for model validation

334 For validation of the model results, we used measurements from two studies: one from a field
335 survey on landfast sea ice at Barrow (Alaska) and one from an experimental study, INTERICE
336 IV, run at the Hamburgische Schiffbau-Versuchsanstalt (HSVA, Hamburg, Germany), where
337 sea ice was grown in an experimental basin under controlled conditions.

338

339 The field survey at Barrow (near the Barrow sea ice observatory - Geophysical Institute of the
340 University of Alaska, Fairbanks) lasted from January to June 2009, hence, during the whole sea

ice growth and decay season (see Zhou et al., submitted for a complete description). Each month, ice cores were extracted on 1 to 3 occasions for a total of 10 stations. Physical and biogeochemical properties of the extracted ice cores were measured. Sea ice thickness was between 70 and 140 cm and snow depth was between 0 and 40 cm. Columnar ice was dominant, given the spatial homogeneity of the sampling site. We ordered stations that are representative of three main phases in sea ice dynamics: (1) winter stations (e.g. February 2) characterized by strong temperature gradients, typical C-shape salinity profiles and brine volume fraction < 5% (hence low permeability; Golden et al., 1998) except at the bottom; (2) early and mid-spring stations (e.g. March 31 and April 10) when sea ice is thicker but the brine volume fraction is still mainly < 5% and (3) late spring stations (e.g. May 8 and June 5) when the air temperature increase deeply affected the temperature and salinity profiles (see Figure 5 of Zhou et al., submitted for salinity, temperature and brine volume vertical profiles at Barrow, Alaska). The brine volume fraction was higher for late spring stations (up to 25%) suggesting a higher permeability. According to Zhou et al. (submitted), full-depth convection occurred in sea ice brines between mid-spring and late spring stations (between April 10 and May 8), strongly influencing sea ice biogeochemical properties.

The INTERICE IV experimental study at Hamburg took place in an indoor tank (the Arctic Environmental Test Basin of the Hamburg Ship Model Basin, HSVA-Hamburg, Germany) in September-October 2009. The tank is 30 m long, 6 m wide and 1 m deep. 24 polyethylene containers were placed in the tank; each of them accommodating 1 m^3 of North Sea seawater. The air temperature was kept at -15 °C during the initial ice growth period (September 4 to 17). After the sampling on September 17, when ice thickness had reached about 20 cm, the air temperature was increased and kept at -1 °C for the rest of the experiment. Sea ice blocks were sampled at regular intervals, using a specific extraction method to prevent brine drainage

366 (Cottier et al., 1999). As for ice cores from Barrow, the temperature, salinity and other
367 biogeochemical properties were measured, including Ar concentration in the ice (Crabeck et al.,
368 in preparation). Three distinct stages were observed: (1) the initial growth (e.g. September 9)
369 when sea ice brine volume fraction was always > 10%, (2) the growing stage (e.g. September
370 14 and 17) when the brine volume fraction decreased to values close to 5% (except in the
371 bottom of the ice), and finally (3) the decay (warming) phase (e.g. September 21) when the
372 whole ice core brine volume fraction increased to about 10%. The INTERICE IV experiment
373 therefore provides the characteristics of the early growing ice stage (which should be
374 representative of the autumnal sea ice or new lead growth), not captured during the field survey
375 at Barrow.

376

377 ### 3.2. Forcing and initialization

378 The model is run with a 1 h time step at both sites. At Point Barrow, the simulation is
379 performed from January 16 to June 30, 2009. Simulation starts on January 16 because this
380 corresponds to the first ice thickness and snow depth measurements. Atmospheric forcings are a
381 combination of various atmospheric reanalysis and climatologies (Goosse, 1997;
382 Vancoppenolle et al., 2010) using atmospheric fields from the geographical coordinates of the
383 Point Barrow sea ice observation station in 2009 (71.3°N, 156.8°W). Snowfall is retrieved from
384 ECMWF ERA-Interim reanalyses and forecasts (Simmons et al., 2007). Oceanic flux is
385 prescribed (3.3 W m^{-2}) in order to match sea ice thickness and snow depth observations. Initial
386 conditions of the model at Point Barrow are h_i = 0.70 m, h_s = 0.06 m (based on observations)
387 and S = 5.92 ‰ at each depth, based on the bulk salinity versus thickness observation-based
388 regression of Kovacs (1996). The initial surface temperature is set to T^{su} = 265 K.

389

At INTERICE, the simulation is run from September 9 to September 22, 2009. INTERICE forcing is peculiar, since the tank is enclosed in a controlled temperature building. The shortwave radiation is assumed to be nil, as well as the turbulent fluxes, as in a closed building, there is neither sun nor wind. The surface energy balance is therefore reducing to the equilibrium between incoming and outgoing longwave radiation. No snowfall is considered at INTERICE. Oceanic flux is assumed to be nil in order to match sea ice thickness and snow depth observations. Because forcing conditions are only available a few hours before the first ice core was sampled, we use observations to initiate sea ice salinity. At INTERICE, initial conditions are: h_i = 0.088 m and S = 9.46 ‰ at each depth. The initial surface temperature is set to T^{su} = 265 K. An initial linear temperature profile within snow and ice is assumed, with the basal interface being at the seawater freezing point.

Initial values for Ar concentration are specified as follows. Sea water Ar concentration was assumed constant in time at 0.018 mol m^3 for both Barrow and INTERICE, assuming air-sea equilibrium with a reference atmosphere, as described earlier. At Barrow, initial bulk sea ice Ar concentration was considered to follow the ice-ocean salt ratio, i.e. 1/5, to account for brine drainage that occurred during ice formation and neglecting bubble formation before the start of the simulation. At INTERICE, initial bulk sea ice Ar concentration was set to its observed value, i.e. 2.8 mmol m^{-3}. The gas dynamics parameters used for the best (CTRL) run were determined to match as accurately as possible the observed Ar dynamics at the two sites. This was done by adjusting empirically the key parameters for gas dynamics: R^{bub}, α_{sat}, e_T^{gas} and z_{BL} (see Table 1 for the model parameters of the CTRL run).

3.3. Sensitivity experiments

In order to illustrate how the processes represented in the model shape the simulated gas dynamics within sea ice, several sensitivity experiments were performed at the Barrow site (see Table 1 for a description of the model parameters used in all the sensitivity runs). In a first series of sensitivity runs, the sensitivity of simulated Ar concentration to the vertical resolution of the model (runs 01-02) and to initial Ar concentration (runs 03-04) was tested. In a second series of sensitivity runs, the sensitivity of simulated Ar concentration to the key parameters was investigated: the gas bubble nucleation rate R^{bub} (runs 05-07); the gas bubble permeability threshold e_T^{gas} (runs 08-09) and the thickness of the boundary layer z_{BL} used in the parameterization of gas fluxes between sea ice and the atmosphere (runs 10-11). In a third series of sensitivity runs, the model was degraded (i.e. the three major modelled processes: gas bubble nucleation, gas bubble rise and ice-atmosphere gas fluxes were consecutively deactivated) to see the influence of each parameterization (runs 05 and runs 12-13).

4. Results

4.1. Ice growth simulations at Barrow (Alaska)and INTERICE: comparison with observations

At Barrow, modelled sea-ice grows regularly from January to June before maximal ice thickness (i.e. 1.36 m) is attained on May 28 (Figure 1a), which is close to the maximal ice thickness (i.e. ~ 150 cm) observed off Barrow by Nomura et al. (2010a). Simulated snow thickness, which is a result of the balance between snowfall and snow melt, increases from mid-January to May (with a maximum snow height of 0.36 m on April 25). Snow melt starts in May and the snow cover has fully disappeared by June 3. Both the simulated ice thickness and snow depth compare well with observations (black crosses in Figure 1a).

Simulated bulk ice salinity in the upper most layer of the ice remains high from January to mid-May (with salinity ~6) before it reaches a minimum in June (~0.5, Figure 1a). Simulated bulk ice salinity follows the same trend in the lower part of sea ice, with respective salinities of ~9.5 and ~4 from January to June. Simulated temperature in the upper most layer of sea ice evolves from relatively low temperatures in January, February and March (~ -14 °C) to a relative high in June (~ -0 °C). The lowermost layer of sea ice is warmer and evolves from ~ -2.4 °C in January to ~ -1.6 °C in June. During winter and early spring (from January to April 28), the upper two thirds of sea ice are not permeable (with a simulated brine volume $e < 5\%$), while the lower third of the sea ice column is permeable to fluid transport (i.e. with $e > 5\%$). The simulated brine volume compares well with observations during winter and early spring (Figure 2). The permeability of sea ice increased after April 28 (with $e > 5\%$ in the whole ice column), but in the uppermost ice layer (where $e < 10\%$), where flushing freshened the ice near the surface, which hindered the connectivity of sea-ice with the overlying atmosphere (Figure 1). The simulated brine volume compares also well with observations during late spring (Figure 2) but close to the surface of sea ice where the observed brine volume was > 20% while the simulated brine volume was < 10%. Although Zhou et al. (submitted) reported high brine volumes below the top layers of sea ice, they also reported the formation of superimposed ice due to snow melting at the ice surface, hindering gas exchange. This is consistent with the model results. In terms of gas permeability, the brine volume increased above 10% in the whole ice column on June 3, except in the uppermost layer of sea ice (where $e < 10\%$) because of flushing. The uppermost layer brine volume increased above 10% on June 8.

Only two ice types could be distinguished from the vertical profiles of observed ice salinity and temperature at all sites: unflooded cold ice and summer ice. The observed and simulated ice salinity and temperature profiles are presented for Barrow in Figure 3a and b. During ice

463 growth (i.e. from January to May), unflooded cold ice is affected by basal congelation only, salt
464 being trapped in the bottom ice layers and released by gravity drainage in the upper ice layers.
465 Hence, the observed salinity profiles exhibit a typical C-shape while temperature decreases
466 linearly with ice depth. The simulated salinity profiles are reasonably close to observations
467 although slightly overestimated during the ice growth period (Figure 3a). Such discrepancies
468 between the model and observations have already been reported by Vancoppenolle et al. (2010)
469 and may partly be related to imprecise parameterization of heat and salt transfer, as well as to
470 an underestimation of the observed ice salinity by a few g kg^{-1} during *in situ* sampling, where
471 sea ice is warm and highly saline (Notz et al., 2005). Salinity was also underestimated at the
472 surface of sea ice by the model (Figure 3a).
473
474 During summer, snow and ice melt into fresh water that percolates through the brine network
475 and replaces the more saline brine (Vancoppenolle et al., 2007). This flushing of saline brines
476 results in the typical summer ice salinity and temperature profiles observed on June 5. Although
477 the details of the profiles are difficult to reproduce because flushing is a three-dimensional
478 threshold process that depends on snow melt and thus on a good representation of the snow
479 cover, the model seems to represent the seasonality of sea ice salinity and temperature
480 qualitatively well.
481
482 During the INTERICE IV experiment (Figure 1b), sea-ice grows regularly from September 3 to
483 September 22 and maximal simulated ice thickness (i.e. 0.21 m) is attained at the end of the
484 experiment. This is consistent with observations that showed sea ice growing from 4.7 cm on
485 September 4 to 21.2 cm on September 18. No snow was simulated at INTERICE. Simulated
486 and observed salinity, temperature and brine volume at INTERICE are also typical of cold
487 atmospheric conditions, with high ice salinity and low temperature and brine volume in the

upper ice layers (Figure 1b and Figure 4a and b). The whole sea ice cover became permeable at INTERICE along with increasing air temperature on September 17 (month 9.48, Figure 1b).

4.2. Model validation

For simplicity, in the rest of the text, the dissolved Ar, the Ar contained within gas bubbles and the total Ar (i.e. the sum of dissolved Ar and Ar contained in gas bubbles) are redefined by the following expressions:

$$dAR = e\ \zeta^{dAr} \quad \text{eq. 13}$$

$$bAr = C^{bAr} \quad \text{eq. 14}$$

$$TAr = C^{TAr} = bAr + dAr \quad \text{eq. 15}$$

The average results of the CTRL run with respect to *TAr* along with the minimum and maximum simulated *TAr* and the range of observed *TAr* are presented in Figure 5 for the winter, early spring and late spring for Barrow and in Figure 4c for the ice growth period at INTERICE. At Barrow, in winter, the simulated Argon is close to *TAr* observations although slightly overestimating Ar in the lower two thirds of sea ice. In early spring, most *TAr* observations fall between the minimum and maximum simulated *TAr*, although the higher *TAr* concentrations observed in the upper half of the ice cannot be simulated with the model described here. In late spring, the accumulation of *TAr* near the ice surface is represented by the model. *TAr* is, however, slightly underestimated in the lower layers in late spring by the CTRL run. At INTERICE, the *TAr* observations fall within the range of simulated *TAr* in the upper ice layers. *TAr* is slightly overestimated in the lower ice layers. Hence, with a few exceptions, the model presented here represents qualitatively well *TAr* within sea ice at Barrow and INTERICE.

4.3. Simulation of gas dynamics within sea ice

The simulated bulk ice dissolved Ar concentration (*dAr*, mmol Ar m^{-3} of ice), saturation state ($\zeta^{dAr}/\zeta_{sat}^{dAr} * 100$), the simulated amount of Ar contained within gas bubbles (*bAr*, mmol Ar m^{-3} of ice) and simulated total Ar (*TAr*, mmol Ar m^{-3} of ice) are presented for the CTRL run at Barrow and INTERICE (Figure 6a and b). The goal of this section is to describe the general distribution of simulated *TAr* across the ice growing and melting season at the two sites and in relation to the distribution of simulated *dAr* and *bAr*.

At Barrow, the simulated *bAr* accounts for most of the simulated *TAr* variability in the upper layers of sea ice during winter (Figure 6a). Indeed, in the upper layers of sea ice, the simulated *dAr* decreases regularly throughout the simulations (with maximum and minimum *dAr* concentrations of 3.6 and 0.35 mmol m^{-3} of bulk ice, respectively at the beginning of the simulation and at the point when ice starts melting, June 3). As sea ice cools down, the simulated *dAr* concentration increases within brine inclusions and becomes supersaturated. Once the simulated *dAr* is above saturation gas bubbles nucleate and the excess *dAr* is transferred to *bAr*, while the remaining *dAr* follows the Ar solubility line. At Barrow, gas bubbles mostly nucleate in the upper two third of sea ice where simulated saturation levels > 100% are found. The transfer of *dAr* to *bAr* is highest in the middle third of sea ice and the simulated *bAr* mostly accumulates in layer 8 (ice depth = 0.8 * h_i) during winter and early spring because the simulated brine network is not connected and does not allow gas bubbles to escape to the atmosphere. This simulation of gas bubble nucleation, and more particularly of Ar contained within gas bubbles, *bAr*, compares well with the theoretical observations of Ar contained within gas bubbles (subtracting the solubility of Ar to the total Ar measured *in situ*)

during both the winter and early spring (Figure 7). In addition, the model seems to represent *TAr* observations reasonably well during winter and early spring at Barrow (Figure 5).

On the contrary, due to the absence of gas bubbles, the simulated *dAr* accounts for most of the simulated *TAr* variability in the lower layers of sea ice at Barrow during winter (February 3 to April 1) and early spring (April 2 to May 15). In the lower part of sea ice, the simulated *dAr* remains high from the beginning of the simulations (with a concentration of 5.3 mmol m^{-3} of bulk ice on January 16) to the point when ice starts to melt (i.e. with a concentration of 3.2 mmol m^{-3} of bulk ice on June 3, Figure 6) and remains close to its solubility, which explains the absence of gas bubbles. Brine convection in the basal ice layers continuously supplies/removes Ar to/from brine inclusions during ice growth to ensure the continuity of dissolved gas concentration between seawater and brine.

When ice starts to melt and the simulated brine volume increases throughout the ice column, connecting the brine network (on June 3 at Barrow, Figure 1a), the simulated *bAr* starts to migrate upwards (with *bAr* of 30.9 mmol Ar m^{-3} of bulk ice for layer 1, ice depth = 0.1 * h_i, on June 3) because of gas bubble buoyancy. Because the simulated *bAr* migrates upward, the simulated *TAr* is mostly driven by the simulated *dAr* during ice melt (Figure 6). The simulated *dAr* decreases to 0.05 and 1.1 mmol Ar m^{-3} of bulk ice at the end of the simulation in the upper and lower layers of sea ice, respectively. During snow and ice melt in spring, freshwater percolates through the brine network and flushes the saline and Ar concentrated brines towards the underlying ocean, decreasing the simulated *TAr* in all ice layers.

559 At INTERICE, with 2.8 and 9.7 mmol Ar m^{-3} of bulk ice in the upper and lower layers of sea
560 ice during ice growth (i.e. from September 3 to 18), the simulated *dAr* accounts for a major part
561 of *TAr* (Figure 6b). During this period, gas bubbles only formed in the upper half of sea ice and
562 the simulated *bAr* increased up to 0.6 mmol Ar m^{-3} in layer 4 (ice depth = 0.4 * h_i,) on
563 September 17 (Figure 6b), while the simulated *dAr* remained close to its solubility line in the
564 upper ice layers and was continuously resupplied by brine convection in the lower ice layers.
565 The shorter ice growth period between INTERICE (i.e. weeks) and Barrow (i.e. months) may
566 explain the observed difference in the contribution of *bAr* to *TAr*. After air temperature starts to
567 increase on September 18, ice melt has not started yet but gas bubbles migrate towards the
568 surface and the simulated *bAr* accumulates in the uppermost ice layers (with a maximum *bAr* of
569 2.5 mmol Ar m^{-3} of bulk ice). During this period, due to a high porosity in the lower sea ice
570 layers, the simulated *dAr* is still resupplied from the underlying water and stays high (8.4 mmol
571 Ar m^{-3} of bulk ice) while, therefore, the simulated *TAr* is driven by *bAr* and *dAr* in,
572 respectively, the upper and lower ice layers. The model also represents *TAr* observations
573 reasonably well at INTERICE (Figure 4c).

574

575 4.3.1. **Model sensitivity**

576 *4.3.1.1.* ***Sensitivity of total argon to vertical resolution and initial conditions***

577 We first tested the sensitivity of the model to the vertical resolution, i.e. the number of vertical
578 layers used. Sensitivity experiments show that changing the vertical resolution of the model to
579 5 or 20 layers (i.e. runs 5LAY and 20LAY) brings some variability in the shape of the vertical
580 distribution of Ar within sea ice (with shifts in the location and number of Argon peaks, for
581 example), which may be due to either differing timing of vertical transport events or different
582 magnitudes of the vertical fluxes at different resolutions (Figure 8a). However, the changes to

583 the overall total argon content are relatively modest and the main gas dynamics features are
584 captured by all three runs. In the CTRL, 5LAY and 20LAY runs, gas bubbles accumulate in the
585 lower third of sea ice during winter and early spring, and accumulate near the surface of sea ice
586 in late spring. The simulated accumulation of gas bubbles near the surface of the ice in spring is
587 however different between the CTRL, the 5LAY and the 20LAY experiments. In addition,
588 changing the vertical resolution of the model to 5 or 20 layers does not modify significantly the
589 results of the model in terms of argon budget. The differences in total argon terms of tendency
590 (due to ice growth, brine drainage and gas bubble flux) between the CTRL run and the 5LAY
591 and 20LAY runs are less than 5%. In terms of total Argon in sea ice (dissolved + bubbles), the
592 differences between the CTRL and the 5LAY and 20LAY runs are 10.1 and 2.6%, respectively.
593 Finally, a sensitivity analysis to the number of layers shows that, in terms of total Ar within sea
594 ice (TAr), total dissolved Ar (TdAr) and total Ar contained within gas bubbles (TbAr), the
595 model shows small changes with different resolutions (Figure 8b).
596
597 We then tested the sensitivity of the model to initial Ar concentrations. The results of two
598 sensitivity runs (H-INIT and L-INIT, with, respectively, doubled and halved initial CTRL
599 argon concentration, see Table 1) are presented in Figure 9 along with the CTRL run. The
600 simulated argon is significantly higher than observations in the H-INIT run during winter. The
601 CTRL and L-INIT runs better approximate the observed argon concentration at this period of
602 the year. However, for all tested initial Ar concentrations, the model overestimates the
603 accumulation of gas bubbles in the lower third of sea ice, which may be related to uncertainties
604 in the way the model represent some processes such as the gas bubbles nucleation rates (see
605 next section). On the contrary, in early spring, only the CTRL and H-INIT runs give a good
606 estimation of argon throughout sea ice compared to observations, the simulation of argon by the
607 L-INIT run being significantly lower than the observed argon in early spring in the top half of

sea ice. In the lower third of sea ice, the accumulation of gas bubbles is well represented by the three runs in early spring. Finally, in late spring, the three runs all simulate an accumulation of gas bubbles close to the ice surface and all give a fairly good estimation of argon through sea ice. In this context, we are confident that the initialization of argon as done in the CTRL run, i.e. scaling with salinity, is a reasonable choice.

4.3.2. ***Sensitivity of total* argon *to gas bubble nucleation rate***

The results of the sensitivity runs CTRL, BUB1, BUB2 and BUB3 with respect to *TAr* are presented in Figure 10 for winter (February 3 to April 1), early spring (April 2 to May 15) and late spring (the period at which ice started to melt; from June 3 to June 8). These four runs differ in terms of the value of the R^{bub} parameter; the rate at which *dAr* is transferred to gas bubbles (see Table 1 for R^{bub} values). As long as a significant amount of bubbles is not formed in sea ice (i.e. before April 10) the vertically averaged differences between the observations and the BUB1 and BUB2 runs – with respectively no and low nucleation rates – are small (see Table 2). These two runs best represent winter observations, with *TAr* concentrations lying on the dilution line, e.g., varying similarly as ice salinity, assuming the same Ar/Salinity ratio in seawater and sea ice (Figure 10). Once the *bAR* becomes significant in early spring, the low and nil R^{bub} rates in BUB1 and BUB2 runs are not large enough to represent the observed accumulation of *TAr* that is present in the bottom layers of sea ice. On April 10 and May 8, the vertical averages of the BUB1 and BUB2 runs underestimate the vertically averaged *TAr* (Table 2). In addition, during late spring, and therefore at the time of ice melt, the accumulation of *bAr* and thus of *TAr* that is observed in the top two layers of sea ice is not represented adequately by the BUB1 run. On the contrary, the BUB2 run results slightly underestimate this accumulation of gas bubbles in the top layers of sea ice and give a good representation of *TAr* in the lower part of sea ice.

633

634 The vertically averaged difference between the observations and the CTRL and BUB3 runs –
635 with respectively mild and high bubble nucleation rates – are high during winter. With such
636 mild or high R^{bub}, *bAr* accumulates within the bottom layers of sea ice (Figure 10) and *TAr* is
637 overestimated in the lower third of the ice (Table 2). The vertically averaged difference
638 between the observed *TAr* and the results of the CTRL and BUB3 runs are small on February 3
639 but relatively high on April 1 (Table 2). For the early spring period, the CTRL run represents
640 adequately the accumulation of Ar in the bottom layers of sea ice (Figure 10). In particular, on
641 April 10, the CTRL run gives the best representation of *TAr* within the sea ice column (Table
642 2), while the run BUB3 overestimates *TAr* (Table 2 and Figure 10). Therefore, the results of the
643 CTRL run seem to give the best representation of *TAr* during the early spring period. In late
644 spring, once the simulated brine network is connected, gas bubbles rise through the ice column.
645 At Barrow, on June 5, the simulated brine network opened in all ice layers but in the uppermost
646 layer, because of the formation of new sea ice due to flushing and snow melting. As a result,
647 *bAr*, and therefore *TAr*, accumulated within the uppermost ice layer (Figure 10). The CTRL and
648 BUB3 runs seem to overestimate this accumulation of *TAr* in the top layer of sea ice during late
649 spring (Figure 10). On the contrary, due to the rapid rise of gas bubbles, the CTRL and BUB3
650 runs both underestimate TAr in the lower layers of sea ice in late spring. Hence, R^{bub}, which
651 governs how much Ar is stored in gas bubbles in late winter and spring, plays a very important
652 role in gas dynamics within sea ice although different R^{bub} seem to give better results at
653 different times of ice growth/melt.

654

655 ### *4.3.3.* ***Sensitivity of gas bubble rise to sea ice permeability***

656 The results of the sensitivity runs CTRL, BUB_RISE1 and BUB_RISE2 with respect to *TAr* are
657 presented in Figure 11 for the winter (February 3 to April 1), early spring (April 2 to May 15)

and late spring (the period at which ice started to melt; from June 3 to June 8). These three runs differ in the brine volume threshold above which gas bubbles rise through the sea ice column, e_T^{gas}. During winter, as brine volume fraction is relatively low, the bubbles do not yet escape out of the ice and vertically averaged differences in *TAr* among the three runs are low. Differences in vertical distribution of *TAr* are however obvious (Figure 11), as the position of the maximum *TAr* corresponds to the location of gas bubble accumulation (i.e., where $e=e_T^{gas}$). If a low value of e_T^{gas} is used (i.e. BUB_RISE1), the position of the maximum is higher in the ice than if a large value is used (i.e. BUB_RISE2). Wherever the *bAr* peak is, the model seems to accumulate too much *TAr* in winter, for all three runs (Figure 11).

During early spring, brine volume fraction is still relatively low (Figure 1) and gas bubbles are blocked within sea ice brines (Figure 5 and 7). As in winter, the position of the maximum *TAr* is determined by e_T^{gas} and is different between all three runs, being higher for a low e_T^{gas} (BUB_RISE1) and lower for a high e_T^{gas} (BUB_RISE2). Contrary to winter, vertically averaged differences in *TAr* are low for all three runs on April 10 (Table 2), when the model seems to best represent *TAr*. However, on May 8, *TAr* is significantly underestimated by the BUB_RISE1 run for which e_T^{gas} is small (i.e. 0.05) and for which gas bubbles have escaped to the atmosphere between April 10 and May 8, a period when $0.05 < e < 0.10$.

During late spring and ice melt, brine volume fraction increases (Figure 1a). Gas bubbles have already escaped to the atmosphere between April 10 and May 8 for the BUB_RISE1 run (with a small $e_T^{gas} = 0.05$), hence vertically averaged *TAr* is not well represented by the results of this run (Figure 11 and Table 2). As seen in the previous section, the results of the CTRL run estimate reasonably well the vertically averaged *TAr* (Figure 11 and Table 2), representing the accumulation of *bAr* in the top layers of sea ice, although it is overestimated. On the contrary,

683 the results of the BUB_RISE2 run, for which e_T^{gas} is large (i.e. 0.15), do not represent well the
684 accumulation of *bAr* in the uppermost layers of sea ice and overestimates *TAr* in the bottom 8
685 layers of sea ice. The sea ice brine volume *e* is still <0.15 and, for this run, gas bubbles are
686 contained within brine inclusions in the bottom layers of sea ice, overestimating *TAr*. On the
687 contrary, because gas bubbles have not yet risen to the ice surface, the BUB_RISE2 run
688 underestimates *TAr* at the ice surface. Therefore, only the CTRL run with e_T^{gas} = 0.10 gives a
689 reasonable estimation of *TAr* distribution in late spring and e_T^{gas}, which determines the vertical
690 position of the maximum bubble concentration during winter, and the time at which gas
691 bubbles rise towards the ice surface and eventually escape to the atmosphere, plays a very
692 important role in gas dynamics within sea ice.

693

694 #### 4.3.4. ***Sensitivity of total Argon to gas exchange formulation***

695 Because no observations of Ar fluxes between sea ice and the atmosphere were available, the
696 sensitivity of the model to the parameterization of ice-atmosphere gas flux needs to be tested
697 indirectly from Ar observations within the ice and more particularly within the top layer of sea
698 ice. The effect of a diffusive gas flux between the ice and the atmosphere is presented in Figure
699 12 for the runs CTRL, DIFF_FLUX1 and DIFF_FLUX2, which differ in the length of the
700 boundary layer (Z_{BL}) used for the ice-atmosphere flux parameterization. The three runs all
701 include gas bubble flux to the atmosphere as described in Table 1. For these three runs, the gas
702 bubble rise threshold, e_T^{gas}, is 0.10 and gas bubbles have not escaped to the atmosphere before
703 June 8. The different Z_{BL} tested (i.e. 10, 50 and 100 mm) all seem to yield reasonable *TAr* with
704 respect to observations during the winter, early spring and late spring (Figure 12 and Table 2)
705 and the difference between the observed and simulated *TAr* is small for all the three runs. In
706 fact, the monthly diffusive flux of Ar to the atmosphere for the CTRL run is 0.02 ± 0.01 mmol
707 Ar m^{-2} which is small compared to the average *TAr* contained within sea ice during the ice

season: 4.39 ± 1.5 mmol Ar m^{-2}. In conclusion, the length of Z_{BL}, which governs fluxes of Ar between sea ice and atmosphere, does not play an important role in gas dynamics within sea ice.

5. Discussion

5.1. Sea ice-atmosphere gas fluxes

A degradation of the model is presented in Figure 13. When gas fluxes between sea ice and the atmosphere are considered to be nil (run NO_FLUX with $Z_{BL} = \infty$, Table 1 and red line in Figure 13), almost no difference exist between these results and those of the CTRL run presented in Figure 5. In addition, the differences between the observed and simulated *TAr* are small for the CTRL run at the two sites studied (Barrow and INTERICE, Table 3). *TAr* is only slightly overestimated at INTERICE (Table 3). We may, therefore, consider that the diffuse type of flux parameterization we used is a reasonable approach to represent *TAr* within sea ice at INTERICE too. It also seems that changes in the parameterization of diffusive gas fluxes between sea ice and the atmosphere are of small importance, possibly because diffusive Ar fluxes between sea ice and the atmosphere were low (averaging 0.02 ± 0.01 mmol Ar m^{-2} at Barrow) during the period studied (i.e. with all samples obtained before or during ice melt).

This is in apparent contradiction with many studies which reported important gas fluxes between sea ice and the atmosphere (Geilfus et al., 2012; Miller et al., 2011b; Nomura et al., 2010a; Papakyriakou and Miller, 2011) although these studies looked at CO_2 fluxes. CO_2 is a biogeochemically active gas which is affected by carbonate chemistry (Geilfus et al., 2012; Miller et al., 2011a), by primary production and respiration (Arrigo et al., 2010; Deming, 2010) and by calcium carbonate precipitation and dissolution (Dieckmann et al., 2008; Dieckmann et

al., 2010) within sea ice. Hence, CO_2 and Ar fluxes between sea ice and the atmosphere may be different. Unfortunately, sea ice-atmosphere Ar fluxes have not been measured *in situ* so far and comparisons must be made with gases other than Ar. In addition, the above cited studies did not differentiate between sea ice-atmosphere fluxes of gases dissolved within brines and gases contained within bubbles. When adding diffusive Ar and gas bubble fluxes, we find that total Ar fluxes were lesser in winter than during ice melt (e.g. in the CTRL simulation at Barrow, the diffusive gas flux was 0.034 and 0.004 mmol Ar m^{-2} in January and June, respectively, while the flux of gas bubbles to the atmosphere was 0 and 3.98 mmol Ar m^{-2} in January and June, respectively). This is consistent with the results of Geilfus et al. (2012) and Miller et al. (2011b) who observed higher CO_2 fluxes in summer than in winter.

Our modelling approach does not take into consideration the effect of wind on gas fluxes between sea ice and the atmosphere. In the field, sea ice-atmosphere gas fluxes measured *in situ* depend on wind and on the physical status of snow and ice (Nomura et al., 2010b). Although it was not necessary in the present study, a modelling effort is needed to constrain the effect of wind and snow on sea ice-atmosphere gas fluxes. To do so, one must consider two different approaches. A first approach should consider the effect of wind speed on sea ice-atmosphere gas fluxes in the presence of a snow cover. Takagi et al. (2005) and Bowling and Massman (2011) showed that CO_2 fluxes between the snow and the atmosphere were enhanced by wind-pumping. In fact, it is possible that, *in situ*, ice-snow gas fluxes are slower processes than snow-atmosphere gas fluxes. The strong gas fluxes reported by the above cited studies may reflect snow-atmosphere gas fluxes rather than ice-atmosphere gas fluxes. A second approach should consider the effect of wind pumping on ice-atmosphere gas fluxes in the absence of a snow cover. To do so one would consider gas exchanges at the ice surface to occur through, centimetres wide brine openings or meters wide melt ponds. However, no parameterization of

this phenomenon exist in the literature and oceanic approaches (e.g. Wanninkhof, 1992) are likely to overestimate sea ice-atmosphere gas fluxes (Loose et al., 2009). To overcome the lack of existing parameterization, the effect of wind on sea-ice atmosphere gas fluxes should be tested with observations.

5.2. Gas bubble rise through the ice column

A situation for which gas bubble rise is considered nil (i.e. $e_T^{gas} = 1$, the run NO_RISE in Table 1) is presented in Figure 13 (green curve). *TAr* is well represented by this run during winter and early spring (with most observations falling near the green curve). However, this configuration presents two caveats. First, in winter and early spring, no layer of high gas concentration is formed, in contrast to observations. Second, with no bubble rise, *TAr* is significantly overestimated during ice melt, when gas bubbles are efficiently transporting Ar towards the surface in the CTRL simulation. This run shows the importance of the parameterization of the gas bubble rise through the ice column. Because of their buoyancy, gas bubbles are expected to rise through the ice column when the brine network is sufficiently connected. Although the presence of gas bubbles within sea ice has been reported before (Light et al., 2003; Tison et al., 2002) their rise through the sea ice column has not been described so far but indirectly by Zhou et al. (submitted) who observed that gas bubbles were only present in the uppermost layer of sea ice when the brine network opened during ice melt.

The commonly accepted brine volume threshold of 5% (Eide and Martin, 1975; Golden et al., 1998) seems too small for gas permeability to reproduce the rise of gas bubbles through sea ice. In run BUB_RISE1 (with $e_T^{gas} = 5\%$, Figure 11), the depth of maximum gas concentration is too high in early spring and the gas loss in late spring occurs too early. A higher threshold (i.e.

781 e_T^{gas} = 10%) as used in the CTRL run gives the best results in terms of *TAr* during winter, early
782 and late spring. This discrepancy may be explained by the tortuosity of sea ice, i.e. the physical
783 structure of brine channels. Brine inclusions are vertical tubular structure attended by smaller
784 tributary channels (Light et al., 2003) within which gas bubbles may get trapped even when 5
785 % < e < 10 %. It should also be noted that the brine volume threshold of 5% is accepted for
786 columnar ice (Golden et al., 1998) but may be higher for other ice types (Ono and Kasai, 1985;
787 Weeks, 2010). This is also in agreement with Loose et al. (2011b) who reported gas diffusion to
788 occur through young sea ice for brine volume fractions between 6.1 and 7.9%. A higher gas
789 bubble permeability threshold (e_T^{gas} = 15%, as used in BUB_RISE2, Figure 11) spuriously
790 blocks *TAr* both in winter, deep into the ice; and in summer, after the observations suggest
791 significant argon depletion in the lower layers of sea ice. Such a value is therefore not adapted
792 to represent gas bubble rise in the model used here. Observations of the depth of the maximum
793 gas concentration in late winter, as well as a precise characterization of the ice temperature,
794 salinity, gas bubbles and brine inclusions properties may help to better understand this
795 important process.

796

797 The accumulation of argon near the ice surface during late spring seems to be well represented,
798 although overestimated, by the rise of gas bubbles when the 10% permeability threshold is used
799 (CTRL run, Figure 11). However, other phenomena may explain the accumulation of argon at
800 that stage of ice melt. First, following brine drainage, the Ar may have originated from a direct
801 input of atmospheric air into ice pores (through void formation; Light et al., 2003). Second, the
802 accumulation of Ar may have been related to the filling of ice pores by snow melt water
803 followed by rapid freezing. Zhou et al. (submitted) provide evidence that the measured
804 concentration of Ar in the top layer of sea ice on June 5 (equivalent to 0.29 ml Ar L_{ice}^{-1} in
805 standard temperature and pressure,STP) was similar to the argon concentration obtained from

806 the instant freezing of seawater (0.23 ml Ar L_{ice}^{-1} in STP) (Matsuo and Miyake, 1966). Zhou et
807 al. (submitted) concluded that gas accumulation is possible through the formation of
808 superimposed ice (snow melt with subsequent freezing at the ice interface). This calls for more
809 observations and modelling studies.
810
811 It should also be noted that, although the model simulates the position of the maximum gas
812 concentration with this 10% permeability threshold, the rise of gas bubbles does not give a
813 good representation of TAr in the lower layers of sea ice on June 5 (Figure 11). After this
814 period, the release of gas bubbles to the atmosphere leaves the ice depleted in argon. This is the
815 result of the model design and cannot be verified *in situ* for security reason (i.e. sea ice
816 sampling would become too dangerous after a minimum ice thickness is reached). However,
817 this particular subject should be investigated further. In addition, although we only considered
818 small gas bubbles to nucleate within sea ice in the present study, it is possible that temperature
819 had an effect on gas bubble size and, therefore, an effect on gas bubble rise. For example, if we
820 considered the smallest gas bubbles (i.e. 0.004 mm in diameter) that were reported by Light et
821 al. (2003) for sea ice at -15 °C, their potential rising velocity, calculated from the dirty gas
822 bubbles formula of Woolf and Thorpe (1991), would be 10^{-5} m s^{-1} or 0.05 m h^{-1}. Under these
823 conditions, it is possible that smaller gas bubbles would require more time to rise through the
824 ice column. On the contrary, gas bubbles larger than 0.1 mm may experience significant
825 interaction and viscous drag with the sidewalls of the brine inclusions, modifying gas bubble
826 rise. This may also explain why the brine volume threshold we found appropriate for gas
827 bubble rise (e = 10%) was higher than the previously reported brine volume threshold for other
828 tracers in sea ice (e = 5%; Golden et al., 1998). Future modelling studies should include the size
829 of gas bubbles as a function of temperature and as a parameter to determine the distribution of
830 gas bubbles within sea ice.

Finally, it is possible that tidal currents also play a role on gas bubble movement within sea ice through forced convection (Neufeld, 2008). For instance, Cota et al. (1987) and Cota and Horne (1989) recognized tidal currents to play a role in nutrients supply to the bottom layers of sea ice. However, because this process is not well understood and has not been modelled so far, we call for other modelling studies to evaluate the role of tides on gas dynamics within sea ice.

5.3. Ar transfer between brines and gas bubbles

A situation for which gas bubble nucleation is considered nil is presented in Figure 13 (run BUB1, blue curve). Gas bubbles increase the *TAr* content in winter and early spring, and decrease it in summer. In early winter, gas bubbles have had no time yet to efficiently form in the model; therefore ascribing nucleation to zero does not change the results. Later on, in late winter and early spring, if no gas bubbles form, Ar cannot intensively accumulate at a depth ~2/3 x h_i. In the CTRL simulations with gas bubbles (Figure 5), some Ar from the liquid phase is transferred to bubbles, and simultaneously, brine convection refills brine inclusions in Ar, which induces a net accumulation of Ar within sea ice. This is an Ar-specific form of the brine convective pump evidenced for nutrients by Vancoppenolle et al. (2010). In addition, the run with gas bubble nucleation = 0 does not represent the high *TAr* concentration at the surface of sea ice during ice melt, when gas bubbles accumulate near the surface in the CTRL run. This experiment, therefore, shows the importance of a precise quantification of the rate of gas transfer between brine inclusions and gas bubbles for a proper quantification of gas budget in sea ice, as highlighted by previous studies (Light et al., 2003; Tison et al., 2002).

854 The gas bubble nucleation parameterization used here, transferring a determined percentage of
855 the Ar supersaturation above a saturation threshold of 100%, seems to represent qualitatively
856 well the observed *TAr* depending on the run and the time of the year studied. Some model
857 tuning was necessary and different nucleation rates best constrain Ar dynamics at Barrow at
858 different periods of the sea ice season (with best results brought by the runs BUB1 and BUB2
859 during winter, by the runs CTRL and BUB3 during early spring, and by the runs BUB2 and
860 CTRL during late spring), suggesting variable nucleation rates in the field. Therefore, future
861 studies should focus on better understanding what are the main physical drivers of gas bubble
862 nucleation in sea ice, which should help to design better model parameterizations. In fact, some
863 mechanisms of gas bubble formation not considered here may significantly contribute to gas
864 dynamics in sea ice.
865
866 The characteristics of brine microstructure should likely play a significant role: Jones et al.
867 (1999) suggest that gas bubbles may form even at low supersaturation if gas cavities pre-exist.
868 On the contrary, Killawee et al. (1998) and Tison et al. (2002) noticed that gas bubble
869 nucleation occur at various supersaturation levels depending on convection at the ice water
870 interface and on ice freezing rates. In addition, gas bubbles may form in brine inclusions when
871 lower density ice melts into higher density brine liquid, forming cavities (i.e. voids, Light et al.,
872 2003). The presence of hydrophobic exopolymeric substances excreted by sea ice sympagic
873 organisms (i.e. ice algae and bacteria), and which are abundant in sea ice (Underwood et al.,
874 2010), may also serve as suitable gas bubble nucleation sites. The presence of gap layers
875 (Fritsen et al., 2001; Kattner et al., 2004) within sea ice may also modify gas dynamics and the
876 distribution of gas bubbles within sea ice. In addition, for other gases such as methane, CH_4,
877 gas bubbles may be released from anoxic sediments to the water column (Shakhova and
878 Semiletov, 2007; Shakhova et al., 2009). This is particularly true in the Arctic Ocean where the

879 East Siberian shelves contribute to about 15% of human CH_4 emissions (Shakhova et al., 2009).
880 Finally, gas bubbles had no physical status in the present model because only one gas was
881 described here, which may explain the low transfer rates between *dAr* and *bAr*. These
882 mechanisms may be considered in future modelling attempts.
883

884 ### 5.4. Ocean-ice-atmosphere Ar budget

885 Although Ar is an inert gas (i.e. not affected by biological processes) and is not climatically
886 significant, the seasonal Ar budget between the ocean, sea ice and the atmosphere may well
887 illustrates what are the important processes driving gas concentrations in sea ice. We used our
888 best run (CTRL) at Barrow, to provide a model-based estimate of the contributors to the Ar
889 budget (Figure 14).
890

891 In Figure 14a, it can be observed that sea ice stores some of the oceanic Ar during winter and
892 spring (i.e. January to May) before Ar is released to the atmosphere and the underlying ocean
893 during ice melt (i.e. June). The accumulation of Ar within sea ice is mainly caused by the
894 formation of sea ice during winter and spring (with a maximum flux of 4.2 mmol Ar m^{-2} due to
895 ice growth, Figure 14b) and compares well with the integrated argon concentrations (Figure
896 14a, red crosses) observed by Zhou et al. (submitted). Most of this stored Ar is rejected by
897 convection to the ocean: Ar fluxes from sea ice to the ocean due to brine drainage reach a
898 winter peak at – 3.3 mmol Ar m^{-2} in February (Figure 14b). When ice melts in the summer,
899 brine flushing expels some dissolved Ar to the underlying ocean (- 1.3 mmol Ar m^{-2}) while ice
900 melt induces a small loss of Ar to the ocean (- 0.17 mmol Ar m^{-2}). Finally, a large amount of
901 Ar is released to the atmosphere *via* the rising of gas bubbles through the ice column and their
902 release to the atmosphere in June (i.e. – 4 mmol Ar m^{-2}).

903

904 The rapid outgassing of gas bubbles observed here can be related to the higher CO_2 effluxes
905 (i.e. towards the atmosphere) observed by Miller et al. (2011b) in the summer (i.e. April to
906 June) compared to the winter, probably in relation to a higher brine connectivity observed in the
907 summer even though summer wind speeds were lower than those observed during winter. This
908 outgassing of gas bubbles could also be related to the important CO_2 flux to the atmosphere
909 noticed by Nomura et al. (2010a) on May 23 2008 on landfast first year sea ice off Barrow just
910 before sea ice became a CO_2 sink. Compared to other sampling dates, the replicate flux
911 measurements showed a great variation due to a substantial air temperature increase that day
912 compared to other days. Finally, this outgassing of gas bubbles could also be related to the
913 positive CO_2 flux (i.e. towards the atmosphere) that Geilfus et al. (2012) observed as ice
914 temperature increased from -10 to -6 °C before sea ice became a CO_2 sink. Geilfus et al. (2012)
915 observed ice-atmospheric CO_2 fluxes when ice temperature was above -11 °C, which he
916 attributed to ice physics and particularly to higher sea ice brines volume and brine connectivity.
917 The importance of gas bubble escape to the atmosphere in terms of gas fluxes between sea ice
918 and the atmosphere has not been considered so far and calls for more field studies.

919

920 Diffusive Ar fluxes between sea ice and the atmosphere only account for a very small portion
921 of the Ar fluxes between sea ice, the underlying ocean and the atmosphere (with a maximum
922 monthly flux of –0.04 mmol Ar m^{-2} in January). This could be due to the lack of a wind
923 pumping type of parameterization in the present study and which should be developed in future
924 studies. However, sensitivity analyses showed that the observed Ar concentrations within sea
925 ice are well represented by a diffusive type of Ar flux between sea ice and the atmosphere
926 (Figure 12). It is possible that the high sea ice-atmosphere gas fluxes reported in the literature

are also related to gas fluxes between ice-free waters and the atmosphere at a time of the year when sea ice is retreating.

6. Conclusion

This study presents the modelling of the basic processes that govern the dynamics of an abiotic gas within first year sea ice. From this study, it appears that a proper model representation of gas bubble nucleation and rise is necessary to realistically capture the seasonality of Ar dynamics within sea ice. The predictions of total argon distribution in winter and early spring are sensitive to the initial concentration of Argon, which is poorly constrained based on the present state of knowledge and observations. As winter ice-atmosphere gas fluxes (not including gas bubble fluxes) are potentially small, a simple diffusive formulation for ice-atmosphere gas fluxes was sufficient to represent Ar distribution within sea ice, and not very influential. Wind-driven outgassing may occur in reality, but such a parameterization was not needed for a proper representation of vertical distribution of Ar in sea ice. Finally, Ar dynamics appear to be dominated by ice growth and brine drainage during winter and early spring; and by an intense and rapid release of gas bubbles to the atmosphere during spring. This release is much higher than the diffusive ice-atmosphere Ar flux, simulated during ice melt. Our study calls for more observational studies of gas bubble dynamics in sea ice.

7. Acknowledgements

We want to thank the F.R.S.-FNRS and Belgian Science Federal Policy Office for funding via FRFC grants no 2.4649.07 and 2.4584.09 and the BIGSOUTH project, respectively. H.G., J.-L. T. and B.D. are senior research associate, research fellow and research associate with the F.R.S.-FNRS. This is MARE contribution 222. M. V. acknowledges support via FP7 grant

BISICLO. Part of the work described in this report was supported by the European Community's Sixth Framework Programme through the grant to the budget of the Integrated Infrastructure Initiative HYDRALAB III, Contract no. 022441(RII3). The authors would like to thank the Hamburg Ship Model Basin (HSVA), especially Kalle Evers and the ice tank crew, for the hospitality, technical and scientific support and the professional execution of the test programme in the Research Infrastructure ARCTECLAB.

8. References

Arrigo, K., Mock, T., Lizotte, M., 2010. Primary producers and sea ice, in: Thomas, D.N., Dieckmann, G.S. (Eds.), Sea Ice. Wiley-Blackwell, Oxford, UK, pp. 282–325.

Bitz, C.M., Lipscomb, W.H., 1999. An energy-conserving thermodynamic model of sea ice. J Geophys Res C: Oceans 104, 15669-15677.

Blanchard, D.C., Woodcock, A.H., 1957. Bubble formation and modification in the sea and its meteorological significance. Tellus A 9, 145-158.

Bowling, D.R., Massman, W.J., 2011. Persistent wind-induced enhancement of diffusive CO2 transport in a mountain forest snowpack. J Geophys Res G: Biogeo 116.

Broecker, W.S., Peng, T.H., 1974. Gas exchange rates between air and sea. Tellus 26, 21-35.

Carte, A.E., 1961. Air bubbles in ice. Proc Phy Soc 77, 757-768.

Comiso, J.C., Nishio, F., 2008. Trends in the sea ice cover using enhanced and compatible AMSR-E, SSM/I, and SMMR data. J Geophys Res C: Oceans 113.

Cota, G.F., 1987. Nutrient fluxes during extended blooms of Arctic ice algae. Journal of Geophysical Research 92, 1951-1962.

Cota, G.F., Horne, E.P.W., 1989. Physical control of Arctic ice algal production. Mar. Ecol. Prog. Ser. 52, 111-121.

Cottier, F., Eicken, H., Wadhams, P., 1999. Linkages between salinity and brine channel distribution in young sea ice. J Geophys Res C: Oceans 104, 15859-15871.

Delille, B., Jourdain, B., Borges, A.V., Tison, J.L., Delille, D., 2007. Biogas (CO2, O2, dimethylsulfide) dynamics in spring Antarctic fast ice. Limnol. Oceanogr. 52, 1367-1379.

Deming, J.W., 2010. Sea ice bacteria and viruses, in: Thomas, D.N., Dieckmann, G.S. (Eds.), Sea Ice. Wiley-Blackwell, Oxford, UK, pp. 247-282.

Dieckmann, G.S., Nehrke, G., Papadimitriou, S., Göttlicher, J., Steininger, R., Kennedy, H., Wolf-Gladrow, D., Thomas, D.N., 2008. Calcium carbonate as ikaite crystals in Antarctic sea ice. Geophys. Res. Lett. 35.

Dieckmann, G.S., Nehrke, G., Uhlig, C., Göttlicher, J., Gerland, S., Granskog, M.A., Thomas, D.N., 2010. Brief communication: Ikaite (CaCO3*6H2O) discovered in Arctic sea ice. Cryosphere Discuss 4, 153-161.

Eide, L., Martin, S., 1975. The formation of brine drainage features in young sea ice. J Glaciol 14, 137-154.

Fritsen, C.H., Coale, S.L., Neenan, D.R., Gibson, A.H., Garrison, D.L., 2001. Biomass, production and microhabitat characteristics near the freeboard of ice floes in the Ross Sea, Antartica, during the austral summer. Ann Glaciol 33, 280-286.

Gat, J.R., Shatkay, M., 1991. Gas exchange with saline waters. Limnol. Oceanogr. 36, 988-997.

Gavrilo, V.P., Gaitskhoki, B.Y., 1970. The statistics of air inclusions in ice, in: V. V., B. (Ed.), The Physics of Ice. Israel Program for Scientific Translation, Jerusalem, pp. 125-128.
Geilfus, N.X., Carnat, G., Papakyriakou, T., Tison, J.L., Else, B., Thomas, H., Shadwick, E., Delille, B., 2012. Dynamics of pCO_2 and related air-ice CO_2 fluxes in the Arctic coastal zone (Amundsen Gulf, Beaufort Sea). J Geophys Res C: Oceans 117.
Gleitz, M., Loeff, M.R.V.D., Thomas, D.N., Dieckmann, G.S., Millero, F.J., 1995. Comparison of summer and winter inorganic carbon, oxygen and nutrient concentrations in Antarctic sea ice brine. Mar. Chem. 51, 81-91.
Golden, K.M., Ackley, S.F., Lytle, V.I., 1998. The percolation phase transition in sea ice. Science 282, 2238-2241.
Goosse, H., 1997. Modeling the large-scale behavior of the coupled ocean-sea ice system. Université Catholique de Louvain, Louvain-la-Neuve, Belgium.
Goosse, H., Fichefet, T., 1999. Importance of ice-ocean interactions for the global ocean circulation: A model study. J Geophys Res C: Oceans 104, 23337-23355.
Grenfell, T.C., 1983. A theoretical model of the optical properties of sea ice in the visible and near infrared. Journal of Geophysical Research 88, 9723-9735.
Hamme, R.C., Emerson, S.R., 2002. Mechanisms controlling the global oceanic distribution of the inert gases argon, nitrogen and neon. Geophys. Res. Lett. 29, 35-31.
Hamme, R.C., Emerson, S.R., 2004. The solubility of neon, nitrogen and argon in distilled water and seawater. Deep Sea Res. (I Oceanogr. Res. Pap.) 51, 1517-1528.
Hamme, R.C., Emerson, S.R., 2006. Constraining bubble dynamics and mixing with dissolved gases: Implications for productivity measurements by oxygen mass balance. J. Mar. Res. 64, 73-95.
Hamme, R.C., Severinghaus, J.P., 2007. Trace gas disequilibria during deep-water formation. Deep Sea Res. (I Oceanogr. Res. Pap.) 54, 939-950.
Ito, T., Hamme, R.C., Emerson, S., 2011. Temporal and spatial variability of noble gas tracers in the North Pacific. J Geophys Res C: Oceans 116.
Jones, S.F., Evans, G.M., Galvin, K.P., 1999. Bubble nucleation from gas cavities - A review. Adv Colloid Interfa 80, 27-50.
Kattner, G., Thomas, D.N., Haas, C., Kennedy, H., Dieckmann, G.S., 2004. Surface ice and gap layers in Antarctic sea ice: Highly productive habitats. Mar. Ecol. Prog. Ser. 277, 1-12.
Keeling, R.F., 1993. On the role of large bubbles in air-sea gas exchange and supersaturation in the ocean. J. Mar. Res. 51, 237-271.
Killawee, J.A., Fairchild, I.J., Tison, J.L., Janssens, L., Lorrain, R., 1998. Segregation of solutes and gases in experimental freezing of dilute solutions: Implications for natural glacial systems. Geochim. Cosmochim. Acta 62, 3637-3655.
Kovacs, A., 1996. Sea ice, part I, bulk salinity versus ice floe thickness, CRREL Report. US Army Cold Regions Research & Engineering Laboratory, Hanover, N.H., p. 16.
Liang, J.H., McWilliams, J.C., Sullivan, P.P., Baschek, B., 2011. Modeling bubbles and dissolved gases in the ocean. J Geophys Res C: Oceans 116.
Light, B., Maykut, G.A., Grenfell, T.C., 2003. Effects of temperature on the microstructure of first-year Arctic sea ice. J Geophys Res C: Oceans 108, 33-31.
Lindsay, R.W., Zhang, J., 2005. The thinning of Arctic sea ice, 1988-2003: Have we passed a tipping point? J. Clim. 18, 4879-4894.
Loose, B., McGillis, W.R., Schlosser, P., Perovich, D., Takahashi, T., 2009. Effects of freezing, growth, and ice cover on gas transport processes in laboratory seawater experiments. Geophys. Res. Lett. 36.
Loose, B., Miller, L.A., Elliott, S., Papakyriakou, T., 2011a. Sea ice biogeochemistry and material transport across the frozen interface. Oceanography 24, 202-218.
Loose, B., Schlosser, P., Perovich, D., Ringelberg, D., Ho, D.T., Takahashi, T., Richter-Menge, J., Reynolds, C.M., McGillis, W.R., Tison, J.L., 2011b. Gas diffusion through columnar laboratory sea ice: Implications for mixed-layer ventilation of CO2 in the seasonal ice zone. Tellus, Series B: Chemical and Physical Meteorology 63, 23-39.

1043 Lubetkin, S.D., 2003. Why is it much easier to nucleate gas bubbles than theory predicts? Langmuir 19,
1044 2575-2587.
1045 Matsuo, S., Miyake, Y., 1966. Gas composition in ice samples from Antarctica. J Geophys Res G: Biogeo
1046 71, 5235-5241.
1047 Miller, L.A., Carnat, G., Else, B.G.T., Sutherland, N., Papakyriakou, T.N., 2011a. Carbonate system
1048 evolution at the Arctic Ocean surface during autumn freeze-up. J Geophys Res C: Oceans 116.
1049 Miller, L.A., Papakyriakou, T.N., Collins, R.E., Deming, J.W., Ehn, J.K., MacDonald, R.W., Mucci, A.,
1050 Owens, O., Raudsepp, M., Sutherland, N., 2011b. Carbon dynamics in sea ice: A winter flux time series.
1051 J Geophys Res C: Oceans 116.
1052 Mock, T., Dieckmann, G.S., Haas, C., Krell, A., Tison, J.L., Belem, A.L., Papadimitriou, S., Thomas, D.N.,
1053 2002. Micro-optodes in sea ice: A new approach to investigate oxygen dynamics during sea ice
1054 formation. Aquat. Microb. Ecol. 29, 297-306.
1055 Nakayama, N., Watanabe, S., Tsunogai, S., 2002. Nitrogen, oxygen and argon dissolved in the northern
1056 North Pacific in early summer. J. Oceanogr. 58, 775-785.
1057 Nemcek, N., Ianson, D., Tortell, P.D., 2008. A high-resolution survey of DMS, CO2, and O2/Ar
1058 distributions in productive coastal waters. Global Biogeochem. Cy. 22.
1059 Neufeld, J., 2008. Natural and forced convection during solidification. Yale University, Yale, p. 186.
1060 Nomura, D., Eicken, H., Gradinger, R., Shirasawa, K., 2010a. Rapid physically driven inversion of the air-
1061 sea ice CO2 flux in the seasonal landfast ice off Barrow, Alaska after onset of surface melt. Cont. Shelf
1062 Res. 30, 1998-2004.
1063 Nomura, D., Yoshikawa-Inoue, H., Toyota, T., Shirasawa, K., 2010b. Effects of snow, snowmelting and
1064 refreezing processes on air-sea-ice CO2 flux. J Glaciol 56, 262-270.
1065 Notz, D., Wettlaufer, J.S., Worster, M.G., 2005. Instruments and Methods A non-destructive method
1066 for measuring the salinity and solid fraction of growing sea ice in situ. J Glaciol 51, 159-166.
1067 Notz, D., Worster, M.G., 2008. In situ measurements of the evolution of young sea ice. J Geophys Res
1068 C: Oceans 113.
1069 Ono, N., Kasai, T., 1985. Surface layer salinity of young sea ice. Ann Glaciol 6, 298-299.
1070 Papadimitriou, S., Kennedy, H., Kattner, G., Dieckmann, G.S., Thomas, D.N., 2003. Experimental
1071 evidence for carbonate precipitation and CO_2 degassing during sea ice formation. Geochim.
1072 Cosmochim. Acta 68, 1749-1761.
1073 Papakyriakou, T., Miller, L., 2011. Springtime CO_2 exchange over seasonal sea ice in the Canadian Arctic
1074 Archipelago. Ann Glaciol 52, 215-224.
1075 Randall, D.A., Wood, R.A., Bony, S., Colman, R., Fichefet, T., Fyfe, J., Kattsov, V., Pitman, A., Shukla, J.,
1076 Srinivasan, J., Stouffer, R.J., Sumi, A., Taylor, K.E., 2007. Cilmate Models and Their Evaluation, in:
1077 Solomon, S., Qin, D., Manning, M., Chen, Z., Marquis, M., Averyt, K.B., Tignor, M., Miller, H.L. (Eds.),
1078 Climate Change 2007: The Physical Science Basis. Contribution of Working Group I to the Fourth
1079 Assessment Report of the Intergovernmental Panel on Climate Change. Cambridge University Press,
1080 Cambridge, United Kingdom and New York, NY, USA.
1081 Rysgaard, S., Bendtsen, J., Delille, B., Dieckmann, G.S., Glud, R.N., Kennedy, H., Mortensen, J.,
1082 Papadimitriou, S., Thomas, D.N., Tison, J.L., 2011. Sea ice contribution to the air-sea CO_2 exchange in
1083 the Arctic and Southern Oceans. Tellus (B Chem. Phys. Meteorol.) 63, 823-830.
1084 Sarmiento, J.L., Gruber, N., 2006. Ocean Biogeochemical Dynamics. Princeton University Press,
1085 Princeton, Woodstock.
1086 Schwerdtfeger, P., 1963. The thermal properties of sea-ice. J Glaciol 4, 789-807.
1087 Semiletov, I., Makshtas, A., Akasofu, S.I., Andreas, E.L., 2004. Atmospheric CO2 balance: The role of
1088 Arctic sea ice. Geophys. Res. Lett. 31, L05121 05121-05124.
1089 Serreze, M.C., Holland, M.M., Stroeve, J., 2007. Perspectives on the Arctic's shrinking sea-ice cover.
1090 Science 315, 1533-1536.
1091 Shakhova, N., Semiletov, I., 2007. Methane release and coastal environment in the East Siberian Arctic
1092 shelf. J. Mar. Syst. 66, 227-243.
1093 Shakhova, N.E., Sergienko, V.I., Semiletov, I.P., 2009. The contribution of the East Siberian shelf to the
1094 modern methane cycle. Herald of the Russian Academy of Sciences 79, 237-246.

Simmons, A., Uppala, S., Dee, D., Kobayashi, S., 2007. ERA-Interim: New ECMWF reanalysis products from 1989 onwards. ECMWF Newsletter 110, 25-35.
Stammerjohn, S.E., Martinson, D.G., Smith, R.C., Iannuzzi, R.A., 2008. Sea ice in the western Antarctic Peninsula region: Spatio-temporal variability from ecological and climate change perspectives. Deep Sea Res. (II Top. Stud. Oceanogr.) 55, 2041- 2058.
Stanley, R.H.R., Jenkins, W.J., Doney, S.C., 2006. Quantifying seasonal air-sea gas exhange processes using noble gas time-series: A design experiment. J. Mar. Res. 64, 267-295.
Takagi, K., Nomura, M., Ashiya, D., Takahashi, H., Sasa, K., Fujinuma, Y., Shibata, H., Akibayashi, Y., Koike, T., 2005. Dynamic carbon dioxide exchange through snowpack by wind-driven mass transfer in a conifer-broadleaf mixed forest in northernmost Japan. Global Biogeochem. Cy. 19, 1-10.
Thomas, D.N., Papadimitriou, S., Michel, C., 2010. Biogeochemistry of sea ice, in: Thomas, D.N., Dieckmann, G.S. (Eds.), Sea Ice. Wiley-Blackwell, London, pp. 425-469.
Tison, J.L., Brabant, F., Dumont, I., Stefels, J., 2010. High-resolution dimethyl sulfide and dimethylsulfoniopropionate time series profiles in decaying summer first-year sea ice at Ice Station Polarstern, western Weddell Sea, Antarctica. J Geophys Res G: Biogeo 115.
Tison, J.L., Haas, C., Gowing, M.M., Sleewaegen, S., Bernard, A., 2002. Tank study of physico-chemical controls on gas content and composition during growth of young sea ice. J Glaciol 48, 177-190.
Tsurikov, V.L., 1979. The formation and composition of the gas content of sea ice. J Glaciol 22, 67-81.
Underwood, G.J.C., Fietz, S., Papadimitriou, S., Thomas, D.N., Dieckmann, G.S., 2010. Distribution and composition of dissolved extracellular polymeric substances (EPS) in Antarctic sea ice. Mar. Ecol. Prog. Ser. 404, 1-19.
Vancoppenolle, M., Bitz, C.M., Fichefet, T., 2007. Summer landfast sea ice desalination at Point Barrow, Alaska: Modeling and observations. J Geophys Res C: Oceans 112.
Vancoppenolle, M., Fichefet, T., Goosse, H., Bouillon, S., Madec, G., Maqueda, M.A.M., 2009. Simulating the mass balance and salinity of Arctic and Antarctic sea ice. 1. Model description and validation. Ocean Model. 27, 33-53.
Vancoppenolle, M., Goosse, H., De Montety, A., Fichefet, T., Tremblay, B., Tison, J.L., 2010. Modeling brine and nutrient dynamics in Antarctic sea ice: The case of dissolved silica. J Geophys Res C: Oceans 115.
Wakatsuchi, M., 1983. Brine exclusion process from growing sea ice. Contributions from the Institute of Low Temperature Science, Hokkaido University, Series A, 29-65.
Wanninkhof, R., 1992. Relationship between wind speed and gas exchange over the ocean. J Geophys Res C: Oceans 97, 7373-7382.
Weeks, W.F., 2010. On sea ice. University of Alsaka, Fairbanks, Alaska.
Woolf, D.K., Thorpe, S.A., 1991. Bubbles and the air-sea exchange of gases in near-saturation conditions. J. Mar. Res. 49, 435-466.
Yager, P.L., Wallace, D.W.R., Johnson, K.M., Smith Jr, W.O., Minnett, P.J., Deming, J.W., 1995. The Northeast Water Polynya as an atmospheric CO_2 sink: a seasonal rectification hypothesis. J Geophys Res C: Oceans 100, 4389-4398.
Zemmelink, H.J., Dacey, J.W.H., Houghton, L., Hintsa, E.J., Liss, P.S., 2008. Dimethylsulfide emissions over the multi-year ice of the western Weddell Sea. Geophys. Res. Lett. 35.
Zemmelink, H.J., Delille, B., Tison, J.L., Hintsa, E.J., Houghton, L., Dacey, J.W.H., 2006. CO2 deposition over the multi-year ice of the western Weddell Sea. Geophys. Res. Lett. 33.
Zhou, J., Delille, B., Brabant, F., Geilfus, N.-X., Tison, J.-L., in preparation. Using O_2/Ar to assess net primary production and its contribution to CO_2 budget in sea ice.
Zhou, J., Delille, B., Geilfus, N.-X., Brabant, F., Eicken, H., Carnat, G., Vancoppenolle, M., Tison, J.-L., submitted. Physical and biogeochemical properties in landfast sea ice (Barrow, Alaska): insights on brine and gas dynamics across seasons. Journal of Geophysical Research.

Figure 1

Click here to download Figure: Fig.1_contours.eps

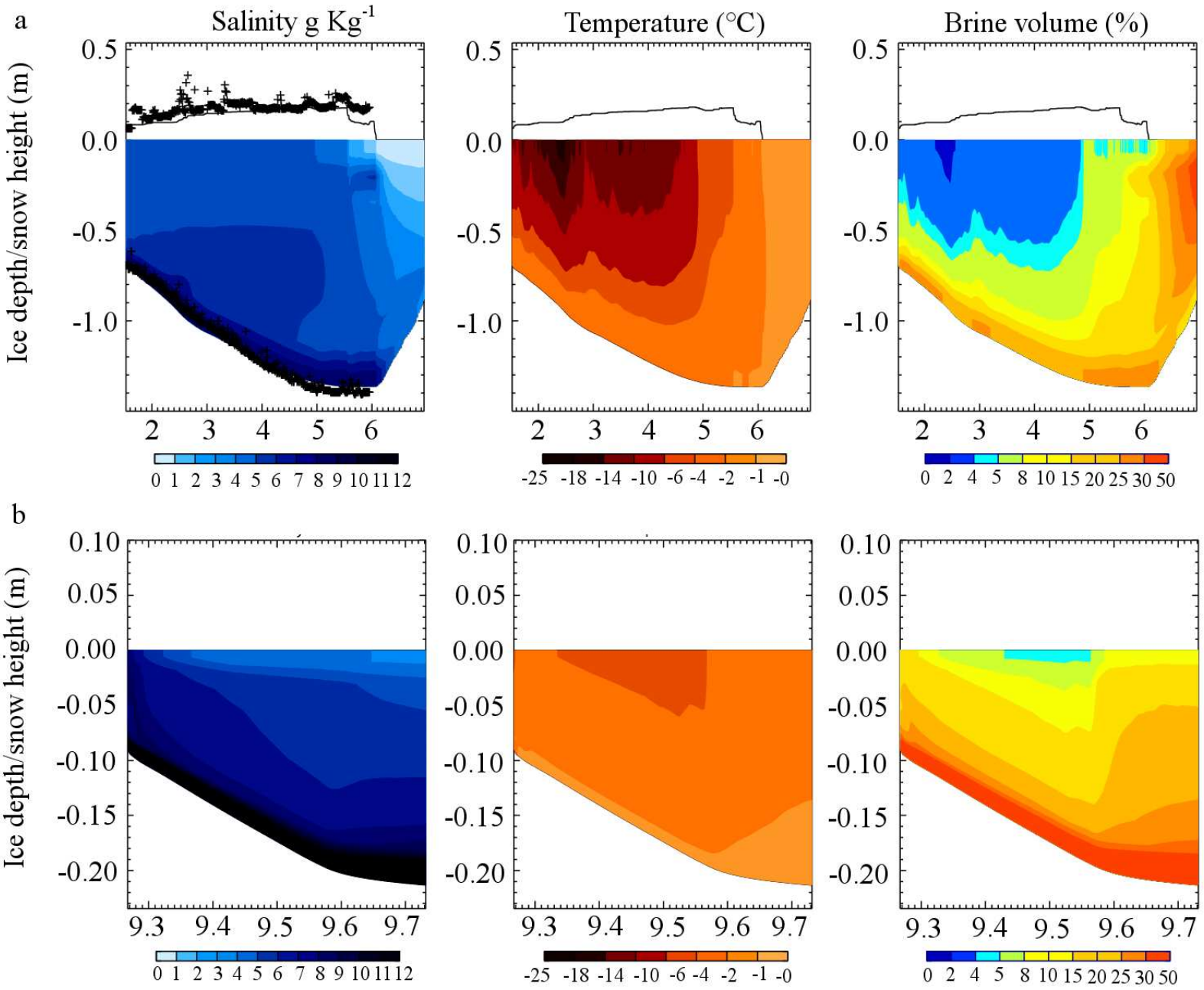

Figure 2

Click here to download Figure: Fig.2.brine_vol.eps

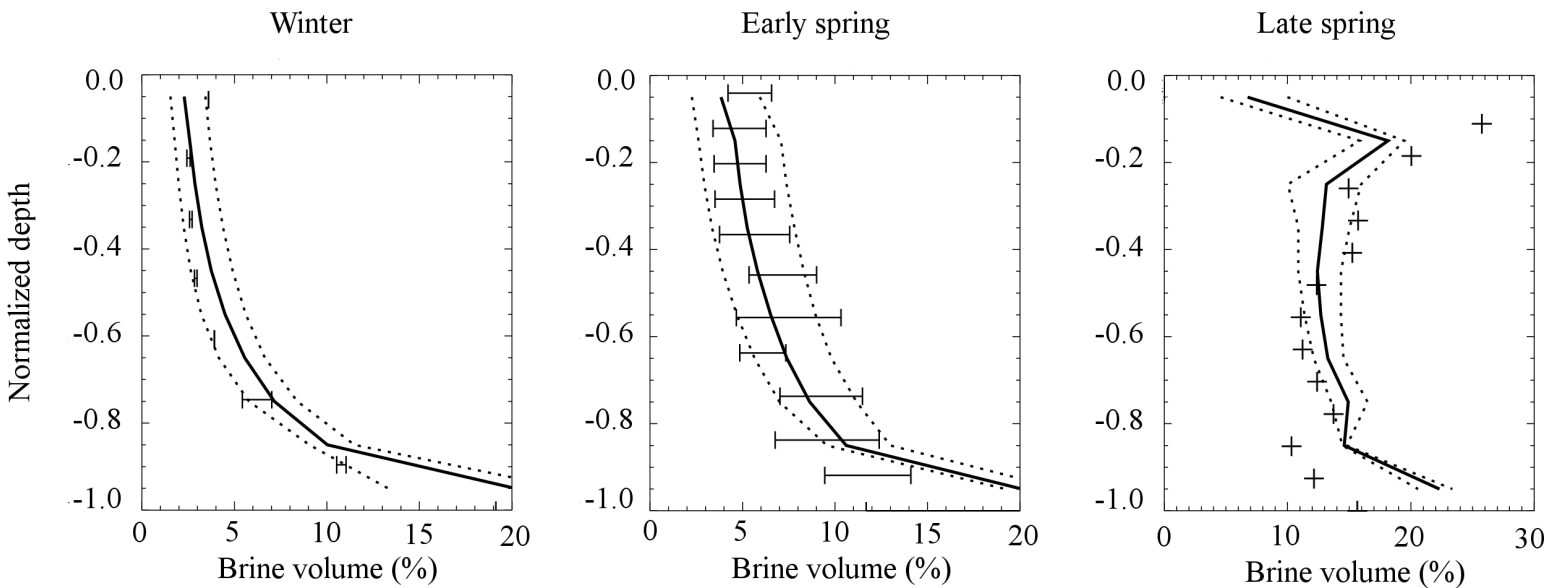

Figure 3

Click here to download Figure: Fig.3.Comparison_model_obs.eps

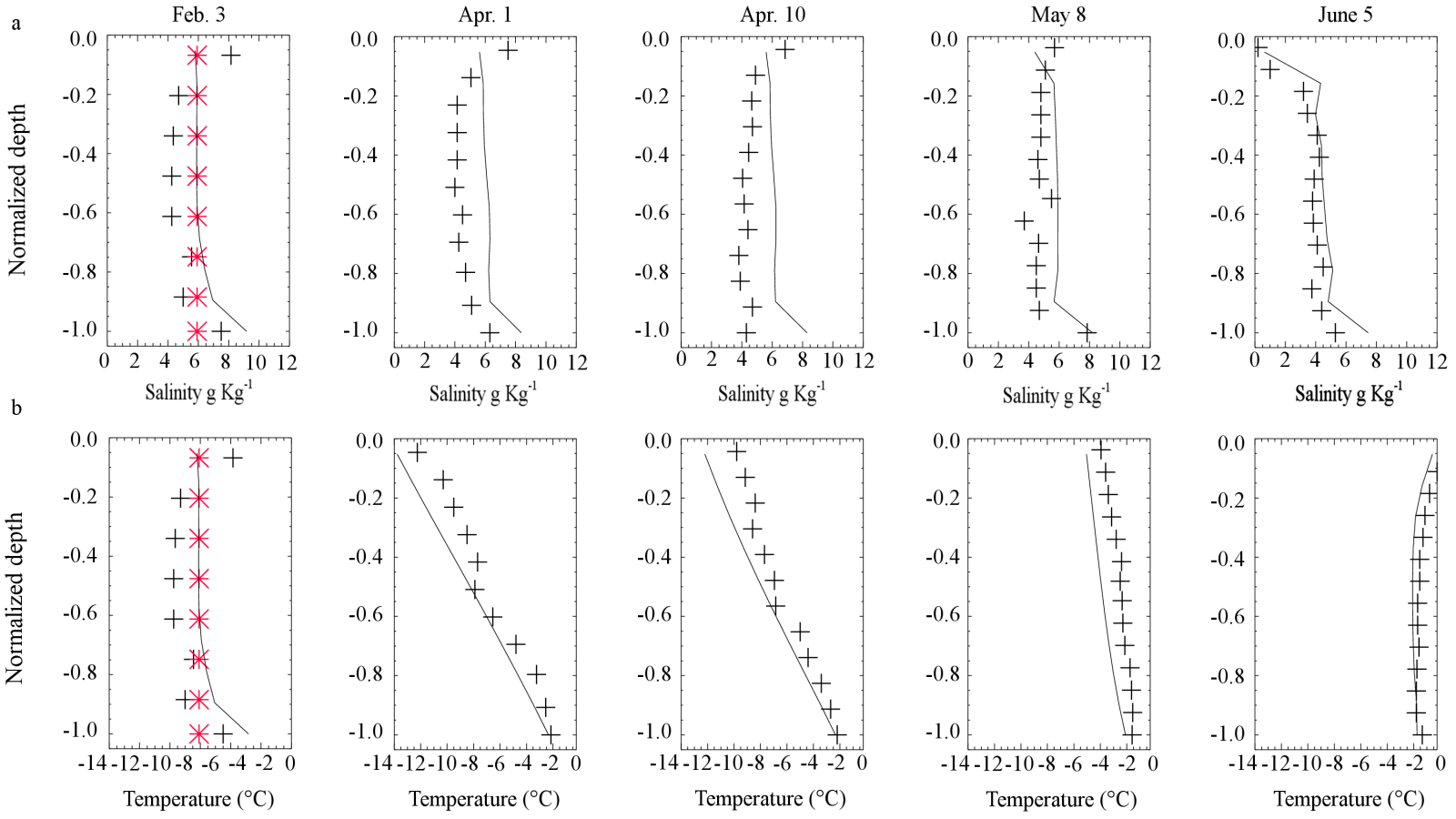

Figure 4

Click here to download Figure: Fig.4.T_S_Ar_Interice.eps

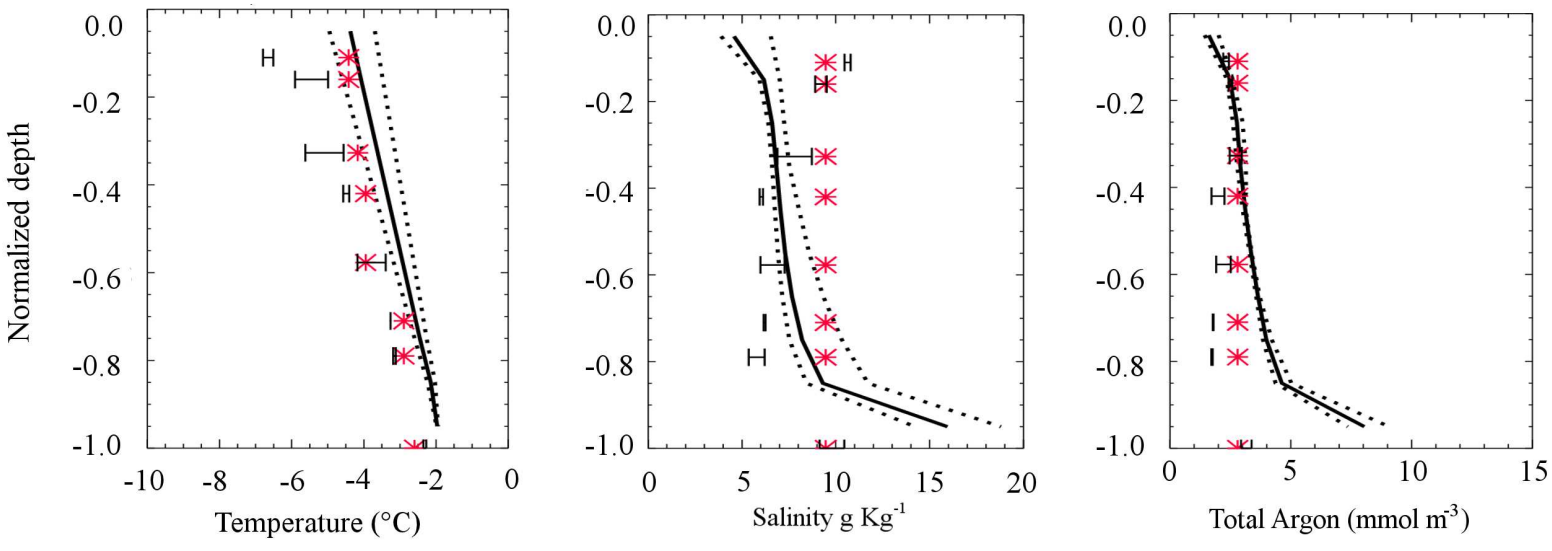

Figure 5

Click here to download Figure: Fig.5.Ar_mod_vs_obs.eps

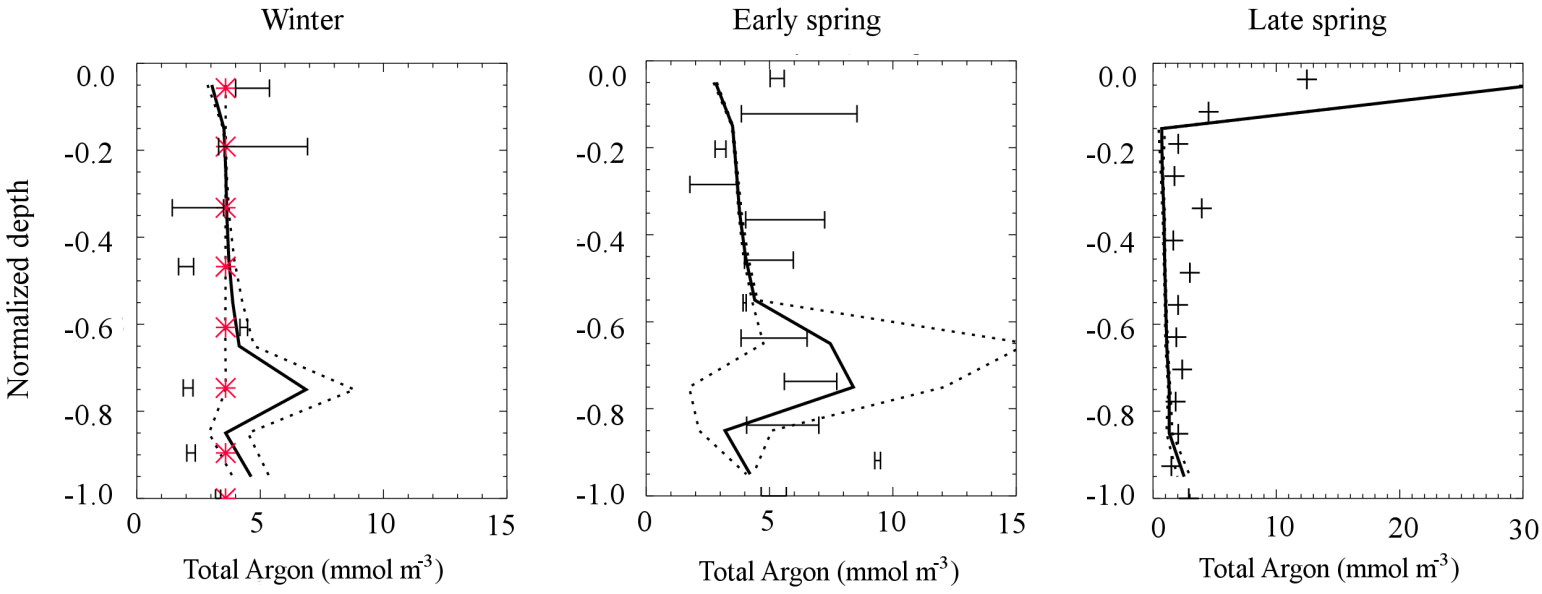

Figure 6

Click here to download Figure: Fig.6_contours.eps

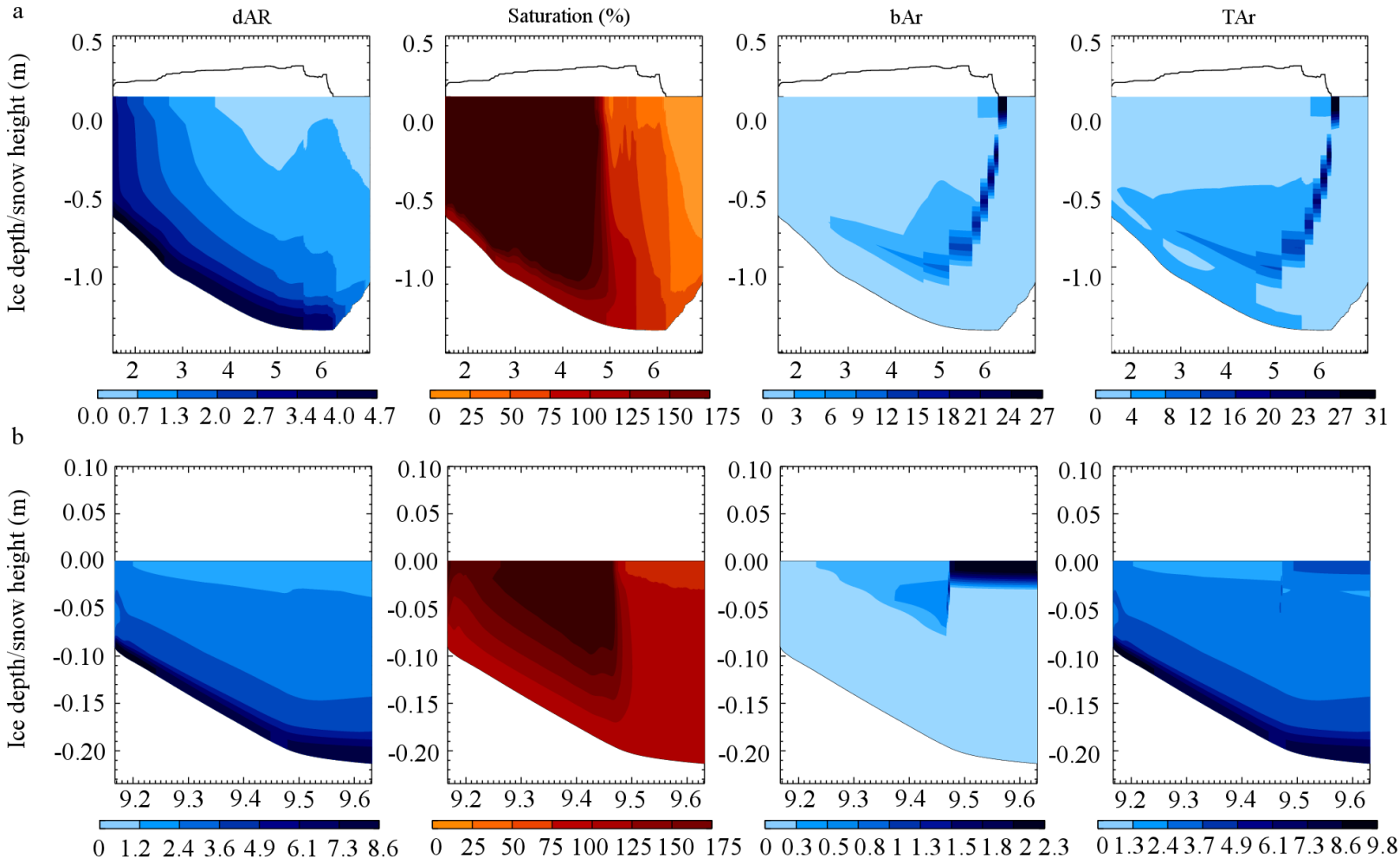

Figure 7

Click here to download Figure: Fig.7.Ar_bubbles_mod_vs_obs.eps

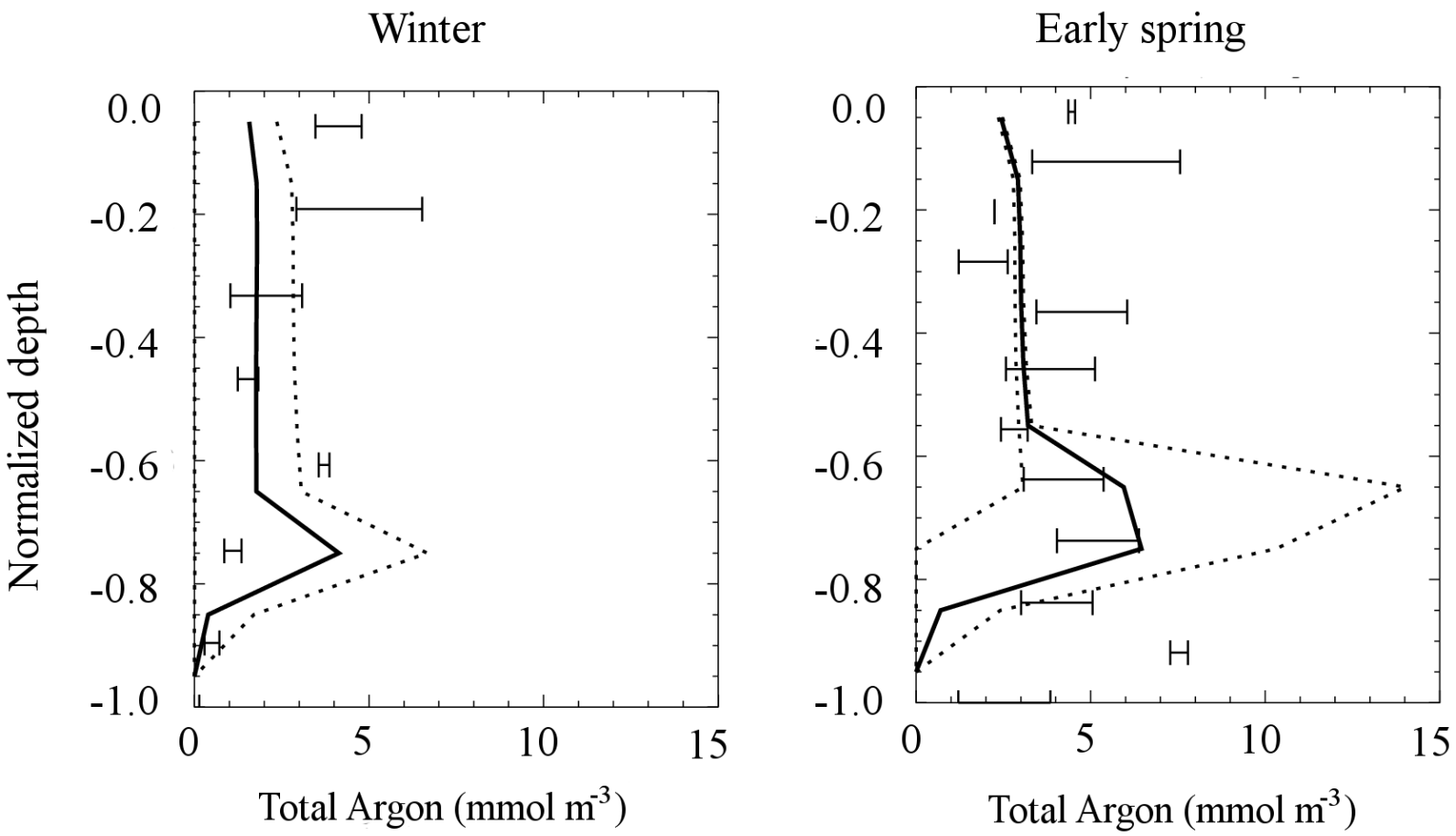

Figure 8

Click here to download Figure: Fig.8.Sensitivity_layers.eps

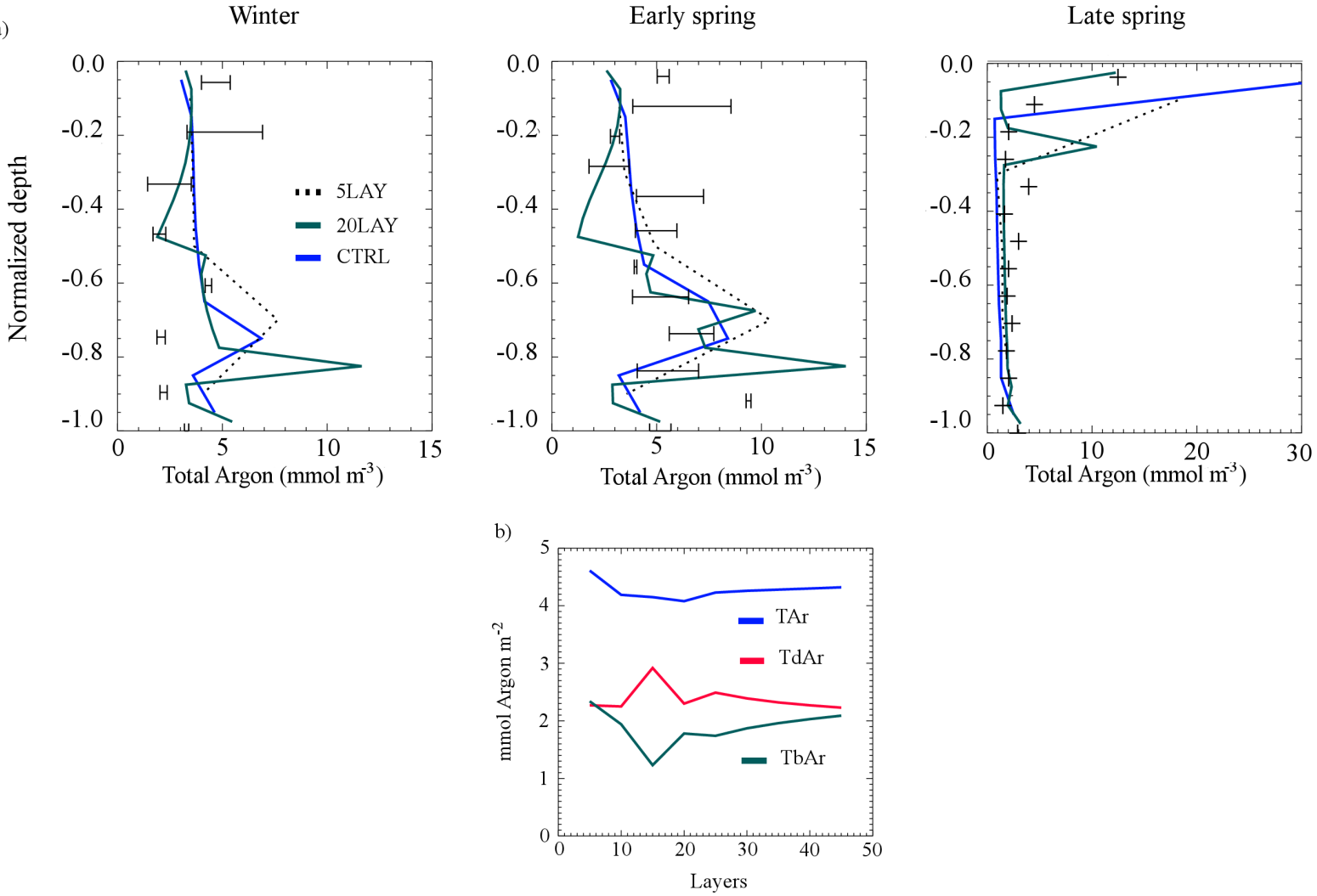

Figure 9

Click here to download Figure: Fig.9.Sensitivity_init_argon.eps

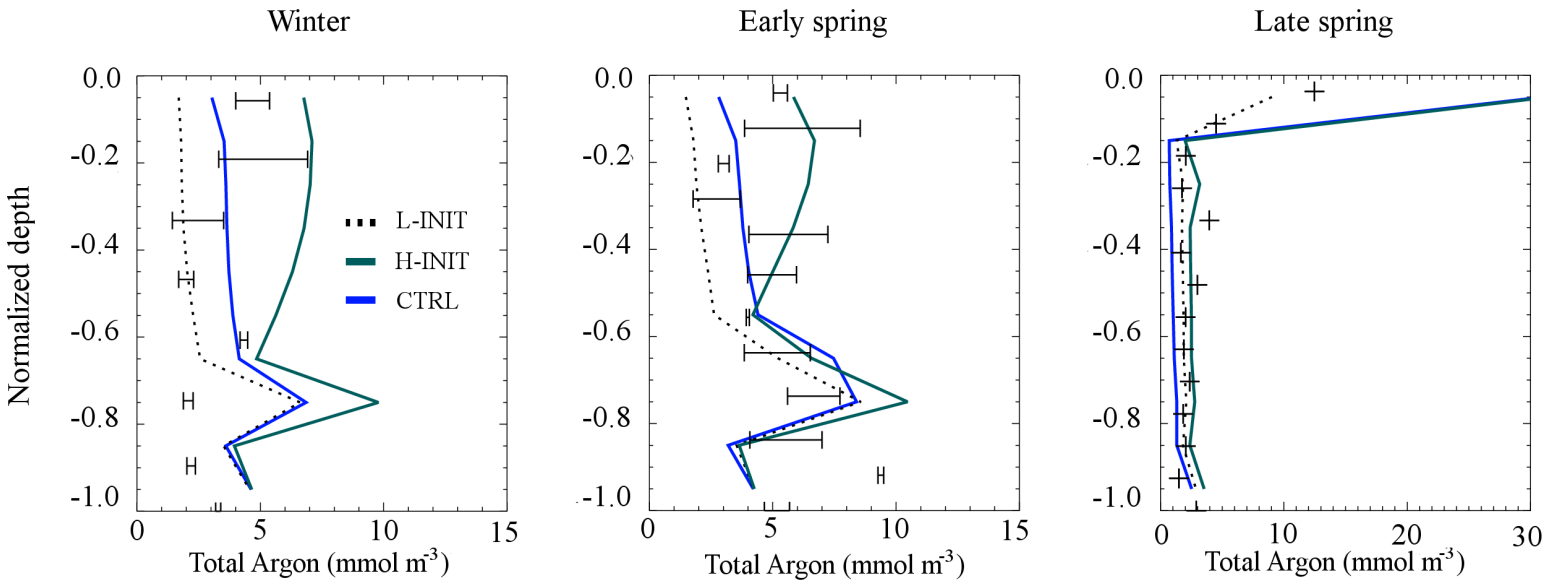

Figure 10

Click here to download Figure: Fig.10.Sensitivity_bub_form.eps

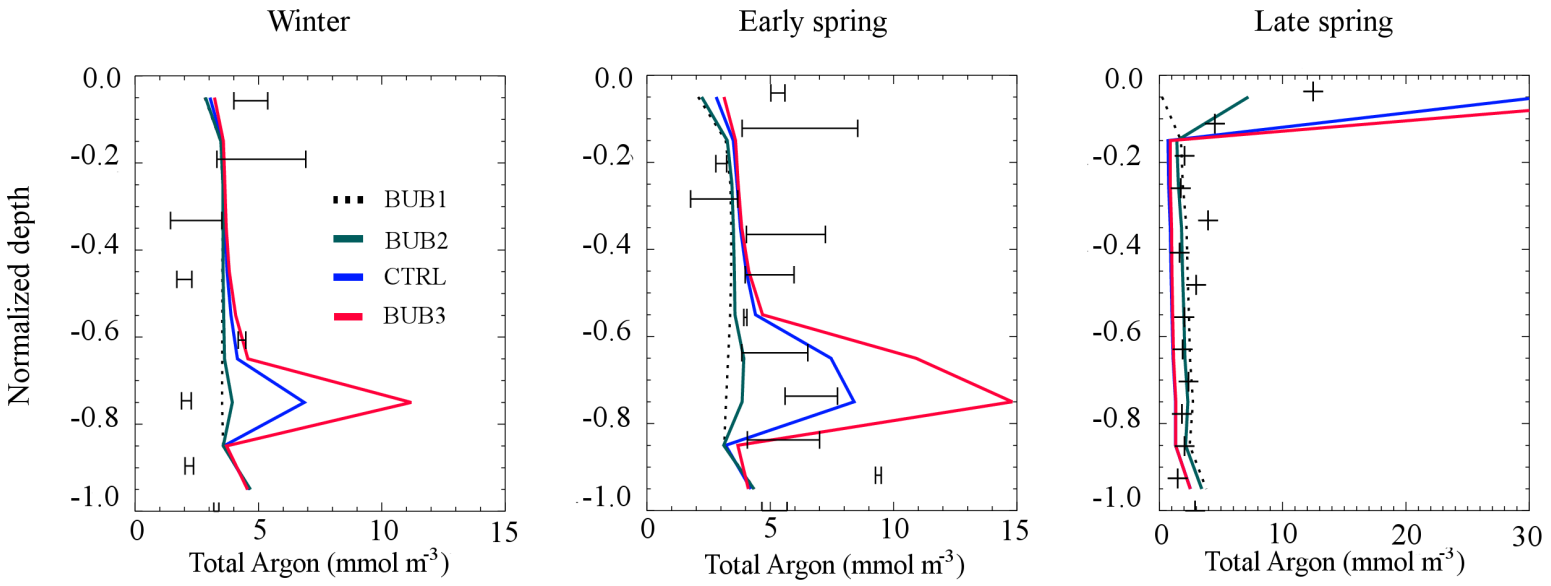

Figure 11

Click here to download Figure: Fig.11.Sensitivity_bub_rise.eps

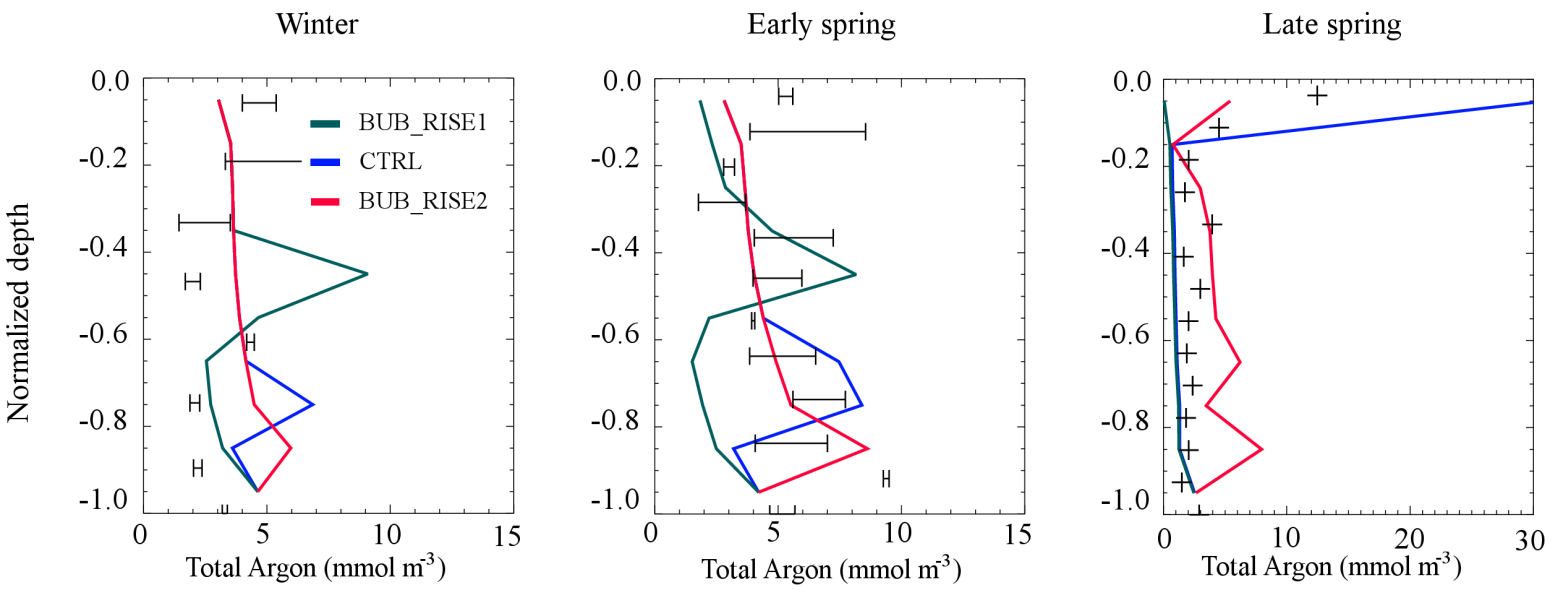

Figure 12

Click here to download Figure: Fig.12.Sensitivity_flux.eps

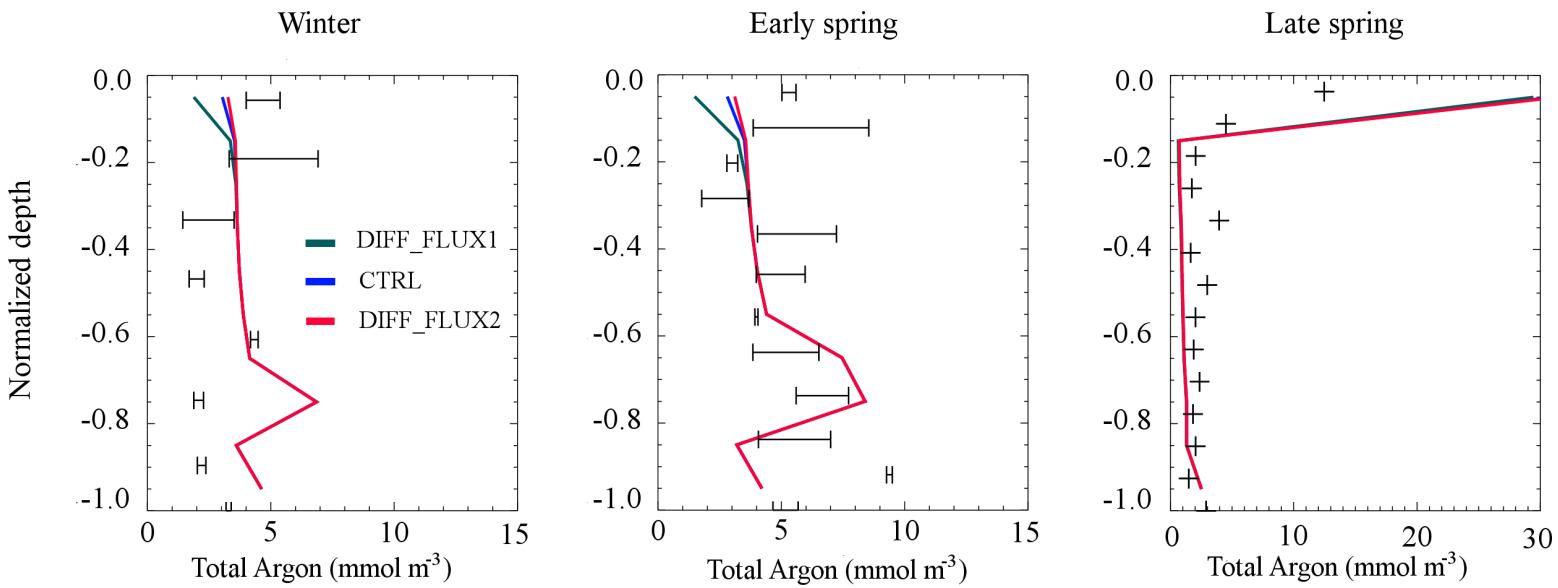

Figure 13

Click here to download Figure: Fig.13.mod_degradation.eps

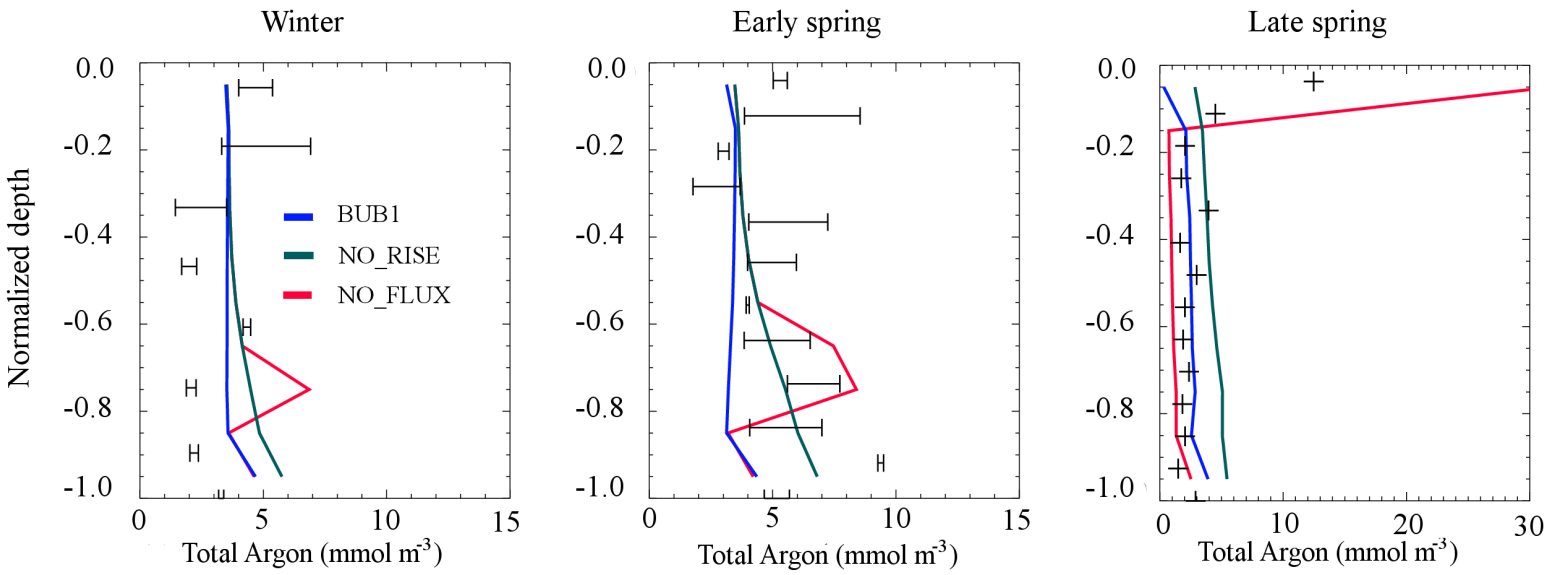

Figure 14

Click here to download Figure: Fig.14_Ar_budget.eps

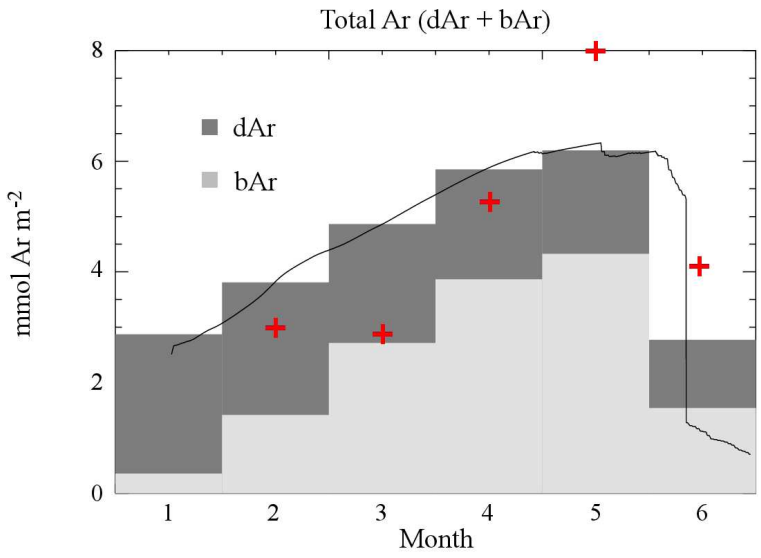

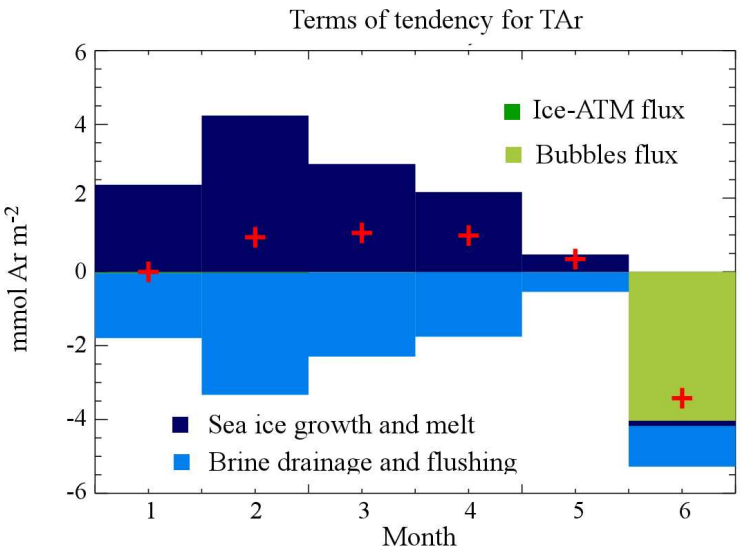

Table

Click here to download Table: Tables.and.figures.legend.doc

Table 1: Sensitivity runs to test the model at Barrow, Alaska. The saturation threshold is $\alpha_{sat=1}$ for all runs.

Run	Name	Nucleation rate	Gas bubble rise	Ice-atmosphere gas flux	Initial Ar concentration	Vertical resolution
00	CTRL	$R^{bub} = 9\ 10^{-2}$ % h^{-1}	$e_T^{gas} = 0.10$	$z_{BL} = 50$ mm	3.6 mmol m^{-3}	10 layers
01	5LAY	$R^{bub} = 9\ 10^{-2}$ % h^{-1}	$e_T^{gas} = 0.10$	$z_{BL} = 50$ mm	3.6 mmol m^{-3}	5 layers
02	20LAY	$R^{bub} = 9\ 10^{-2}$ % h^{-1}	$e_T^{gas} = 0.10$	$z_{BL} = 50$ mm	3.6 mmol m^{-3}	20 layers
03	L-INIT	$R^{bub} = 9\ 10^{-2}$ % h^{-1}	$e_T^{gas} = 0.10$	$z_{BL} = 50$ mm	1.8 mmol m^{-3}	10 layers
04	H-INIT	$R^{bub} = 9\ 10^{-2}$ % h^{-1}	$e_T^{gas} = 0.10$	$z_{BL} = 50$ mm	7.2 mmol m^{-3}	10 layers
05	BUB1	$R^{bub} = 0$ % h^{-1}	$e_T^{gas} = 0.10$	$z_{BL} = 50$ mm	3.6 mmol m^{-3}	10 layers
06	BUB2	$R^{bub} = 10^{-4}$ % h^{-1}	$e_T^{gas} = 0.10$	$z_{BL} = 50$ mm	3.6 mmol m^{-3}	10 layers
07	BUB3	$R^{bub} = 0.25$ % h^{-1}	$e_T^{gas} = 0.10$	$z_{BL} = 50$ mm	3.6 mmol m^{-3}	10 layers
08	BUB_RISE1	$R^{bub} = 9\ 10^{-2}$ % h^{-1}	$e_T^{gas} = 0.05$	$z_{BL} = 50$ mm	3.6 mmol m^{-3}	10 layers
09	BUB_RISE2	$R^{bub} = 9\ 10^{-2}$ % h^{-1}	$e_T^{gas} = 0.15$	$z_{BL} = 50$ mm	3.6 mmol m^{-3}	10 layers
10	DIFF_FLUX1	$R^{bub} = 9\ 10^{-2}$ % h^{-1}	$e_T^{gas} = 0.10$	$z_{BL} = 10$ mm	3.6 mmol m^{-3}	10 layers
11	DIFF_FLUX2	$R^{bub} = 9\ 10^{-2}$ % h^{-1}	$e_T^{gas} = 0.10$	$z_{BL} = 100$ mm	3.6 mmol m^{-3}	10 layers
12	NO_RISE	$R^{bub} = 9\ 10^{-2}$ % h^{-1}	$e_T^{gas} = 1$	$z_{BL} = 50$ mm	3.6 mmol m^{-3}	10 layers
13	NO_FLUX	$R^{bub} = 9\ 10^{-2}$ % h^{-1}	$e_T^{gas} = 0.10$	$z_{BL} = \infty$	3.6 mmol m^{-3}	10 layers

Table 2: Differences between simulated and observed *TAr* concentrations (i.e. Ar dissolved within brines and Ar contained within gas bubbles, *TAr* = *dAr* + *bAr* in mmol Ar m^{-3} of bulk ice) for all the sensitivity runs at Barrow (Alaska). The difference between observed and simulated *TAr* are given as vertical averages of the error ± the standard deviation of the error.

	Barrow (71.3°N, 156.8°W)				
Runs	03-Feb	01-Apr	10- Apr	08-May	05-June
CTRL	-0.48 ± 2.4	1.94 ± 2.2	-0.17 ± 2.8	-1.36 ± 3.9	1.67 ± 8.8
BUB1	-0.49 ± 2.4	0.98 ±1.3	-1.26 ± 2.4	-2.76 ± 2.9	-0.22 ± 1.7
BUB2	-0.49 ± 2.4	1.11 ± 1.3	-1.10 ± 2.4	-2.54 ± 2.8	0.12 ± 1.3
BUB3	-0.48 ± 2.3	2.88 ± 4.1	0.85 ± 4.3	-0.17 ± 7.1	2.92 ± 12.5
BUB_RISE1	-0.21 ± 2.5	1.94 ± 3.7	-0.17 ± 3.7	-4.55 ± 2.8	-1.53 ± 1.4
BUB_RISE2	-0.32 ± 2.5	1.94 ± 1.9	-0.17 ± 1.7	-1.36 ± 2.4	1.66 ± 2.2
DIFF_FLUX2	-0.64 ± 2.6	1.78 ± 2.3	-0.33 ± 2.8	-1.53 ± 4.1	1.49 ± 8.3
DIFF_FLUX1	-0.45 ± 2.3	1.98 ± 2.2	-0.13 ± 2.8	-1.32 ± 3.9	1.71 ± 8.9

Table 3: Differences between simulated and observed *TAr* concentrations for the CTRL run at Barrow and INTERICE. The difference between observed and simulated *TAr* are given at each depth and as vertical averages of the error ± the standard deviation of the error.

	Barrow (71.3°N, 156.8°W)					INTERICE			
depth (m)	03-Feb	01-Apr	10- Apr	08-May	05-June	06-Sep	11- Sep	14- Sep	18- Sep
0.1	-2.53	1.38	-0.03	-6.77	26.52		-0.52	-0.00	-0.49
0.2	-5.15	-1.64	0.81	0.17	-1.23	0.60	-0.03	-0.30	-0.39
0.3	-0.35	2.63	2.27	-0.43	-3.16	0.28	0.64	-0.39	0.02
0.4		2.34	0.39	0.17	-0.71		0.69	1.37	0.62
0.5	1.00	1.93	-3.28	0.03	-2.01				1.06
0.6	-0.93	0.12	0.42	-2.62	-0.84	0.74	1.58	1.46	
0.7	1.25	2.55	-1.65	6.46	-1.21		1.89	1.73	1.53
0.8		7.07	5.45	-2.91	-0.48		2.16	2.11	1.74
0.9	1.49	1.82	-4.48	-7.39	-0.06				
1	1.38	1.22	-1.58	-0.31	-0.14	5.90	4.13	4.61	6.26
Average ± stdev	-0.48 ± 2.4	1.94 ± 2.2	-0.17 ± 2.8	-1.36 ± 3.9	1.67 ± 8.8	1.88 ± 2.7	1.32 ± 1.5	1.32 ± 1.6	1.29 ± 2.2

Figures legend:

Figure 1: Contoured salinity (g kg^{-1}), temperature (° C) and brine volume (%) in the ice domain for the CTRL run at (a) Barrow (Alaska) and (b) INTERICE (an ice tank experiment in Hamburg, Germany). Horizontal and vertical axes refer to months and depth from the snow ice interface, respectively. Black crosses indicate observed snow depth and ice thickness.

Figure 2: Simulated brine volume (%) vertical profiles for the CTRL run and as a function of the normalized depth (z/h_i) during winter (February 3 to April 1), early spring (April 2 to May 15) and late spring along with ice melting (June 3 to June 8). The mean (black line), minimum and maximum (black dotted curve) simulated brine volume are plotted for each period. The mean and standard deviation of observed brine volume for the corresponding periods are plotted (black horizontal lines).

Figure 3: Simulated salinity (g kg^{-1}, a) and temperature (°C, b) vertical profiles for the CTRL run and as a function of the normalized depth (z/h_i) for 5 sampling stations at Barrow (Alaska). Field observations (black crosses) are plotted for comparison with the model. Initial salinity and temperature profiles are also plotted (red crosses).

Figure 4: Simulated temperature (°C), salinity (g kg^{-1}) and *TAr* vertical profiles for the CTRL run and as a function of the normalized depth (z/h_i) for the INTERICE experiment during ice growth (September 4 to 17). The mean (black line), minimum and maximum (black dotted curve) simulated

temperature, salinity and *TAr* are plotted. The mean and standard deviation of observed temperature, salinity and *TAr* for the corresponding period are plotted (black horizontal lines). Initial salinity, temperature and argon profiles are also plotted (red crosses). The profiles are plotted as a function of the normalized depth (z/h_i).

Figure 5: Simulated vertical profiles of *TAr* for the CTRL run at BARROW during winter (February 3 to April 1), early spring (April 2 to May 15) and late spring along with ice melting (June 3 to June 8). The mean (black line), minimum and maximum (black dotted curve) simulated *TAr* are plotted for each period. The mean and standard deviation of observed *TAr* for the corresponding periods are plotted (black horizontal lines). Only one sampling station was performed during early spring and observed *TAr* is represented as black crosses. The initial argon profile is also plotted (red crosses). The profiles are plotted as a function of the normalized depth (z/h_i).

Figure 6: Contoured dissolved Argon concentration (mmol m^{-3} of bulk ice, *dAr*), percent saturation of Ar in brine inclusions (%), Ar quantity present in gas bubbles (mmol m^{-3} of bulk ice, *bAr*) and total Ar (mmol m^{-3} of bulk ice, *TAr*), in the ice domain for the CTRL run at (a) Barrow (Alaska) and (b) INTERICE (an ice tank experiment in Hamburg, Germany). Horizontal and vertical axes refer to months and depth from the snow ice interface, respectively.

Figure 7: Simulated vertical profiles of *bAr* for the CTRL run at BARROW during winter (February 3 to April 1) and early spring (April 2 to May 15. The mean (black line), minimum and maximum (black dotted curve) simulated *bAr* are plotted for each period. The mean and standard deviation

of observed *bAr* (i.e. calculated as the difference between the observed *TAr* and the calculated solubility of Ar) for the corresponding periods are plotted (black horizontal lines). The profiles are plotted as a function of the normalized depth (z/h_i).

Figure 8: a) Simulated vertical profiles of *TAr* at BARROW for the CTRL run (blue curve), and the sensitivity tests 5LAY (black dotted curve) and 20LAY (green curve) during winter (February 3 to April 1), early spring (April 2 to May 15) and late spring along with ice melting (June 3 to June 8). The mean and standard deviation of observed *TAr* for the corresponding periods are plotted (black horizontal lines). Only one sampling station was performed during early spring and observed *TAr* is represented as black crosses. The profiles are plotted as a function of the normalized depth (z/h_i). b) Depth integrated total argon within sea ice (Tar, dissolved + gas bubbles in mmol Ar m^{-2}, blue curve), depth integrated dissolved argon (TdAr in mmol Ar m^{-2}, red curve) and depth integrated gas bubbles argon (TbAR in mmol Ar m^{-2}, green curve).

Figure 9: Simulated vertical profiles of *TAr* at BARROW for the CTRL run (blue curve), and the sensitivity tests L-INI (black dotted curve) and H-INI (green curve) during winter (February 3 to April 1), early spring (April 2 to May 15) and late spring along with ice melting (June 3 to June 8). The mean and standard deviation of observed *TAr* for the corresponding periods are plotted (black horizontal lines). Only one sampling station was performed during early spring and observed *TAr* is represented as black crosses. The profiles are plotted as a function of the normalized depth (z/h_i).

Figure 10: Simulated vertical profiles of *TAr* at BARROW for the CTRL run (blue curve), and the sensitivity tests BUB1 (black dotted curve), BUB2 (green curve) and BUB3 (red curve) during winter (February 3 to April 1), early spring (April 2 to May 15) and late spring along with ice melting

(June 3 to June 8). The mean and standard deviation of observed *TAr* for the corresponding periods are plotted (black horizontal lines). Only one sampling station was performed during early spring and observed *TAr* is represented as black crosses. The profiles are plotted as a function of the normalized depth (z/h_i).

Figure 11: Simulated vertical profiles of *TAr* at BARROW for the CTRL run (blue curve), and the sensitivity tests BUB_RISE1 (green curve) and BUB_RISE2 (red curve) during winter (February 3 to April 1), early spring (April 2 to May 15) and late spring along with ice melting (June 3 to June 8). The mean and standard deviation of observed *TAr* for the corresponding periods are plotted (black horizontal lines). Only one sampling station was performed during early spring and observed *TAr* is represented as black crosses. The profiles are plotted as a function of the normalized depth (z/h_i).

Figure 12: Simulated vertical profiles of *TAr* at BARROW for the CTRL run (blue curve), and the sensitivity tests DIFF_FLUX1 (green curve) and DIFF_FLUX2 (red curve) during winter (February 3 to April 1), early spring (April 2 to May 15) and late spring along with ice melting (June 3 to June 8). The mean and standard deviation of observed *TAr* for the corresponding periods are plotted (black horizontal lines). Only one sampling station was performed during early spring and observed *TAr* is represented as black crosses. The profiles are plotted as a function of the normalized depth (z/h_i).

Figure 13: Simulated vertical profiles of *TAr* for the NO_FLUX (red curve), NO_RISE (green curve) and BUB1 (blue curve) runs at BARROW during winter (February 3 to April 1), early spring (April 2 to May 15) and late spring along with ice melting (June 3 to June 8). The mean and standard deviation of observed *TAr* for the corresponding periods are plotted (black horizontal lines). Only one sampling station was performed during early spring and observed *TAr* is represented as black crosses. The profiles are plotted as a function of the normalized depth (z/h_i).

Figure 14: (a) Monthly budget of vertically integrated *dAr* (dark gray) *bAr* (light gray) for the CTRL run at Barrow (Alaska). The hourly budget of *TAr* (black curve) and the integrated argon concentrations observed *in situ* (red crosses) are indicated. (b) Monthly time integrated flux of *TAr* due to total sea ice growth and melt (dark blue), brine drainage (light blue), ice-atmosphere diffuse Ar flux (dark green) and gas bubble flux (light green) at Barrow (Alaska). The growth and melt of sea ice include the formation of sea ice, the basal growth of sea ice and the surface and basal melt of sea ice. The monthly time integrated ice-atmosphere diffuse argon flux is too low to be observed in the present figure. The red crosses refer to the net monthly changes in *TAr* from the CTRL run at Barrow (Alaska).